



**HAL**  
open science

# The Influence of Grain Size Distribution on Mechanical Compaction and Compaction Localization in Porous Rocks

Lucille Carbillet, Michael J Heap, Patrick Baud, Fabian B Wadsworth,  
Thierry Reuschlé

► **To cite this version:**

Lucille Carbillet, Michael J Heap, Patrick Baud, Fabian B Wadsworth, Thierry Reuschlé. The Influence of Grain Size Distribution on Mechanical Compaction and Compaction Localization in Porous Rocks. *Journal of Geophysical Research: Solid Earth*, 2022, 127 (11), pp.e2022JB025216. 10.1029/2022JB025216 . hal-03845703v2

**HAL Id: hal-03845703**

**<https://hal.science/hal-03845703v2>**

Submitted on 4 May 2023

**HAL** is a multi-disciplinary open access archive for the deposit and dissemination of scientific research documents, whether they are published or not. The documents may come from teaching and research institutions in France or abroad, or from public or private research centers.

L'archive ouverte pluridisciplinaire **HAL**, est destinée au dépôt et à la diffusion de documents scientifiques de niveau recherche, publiés ou non, émanant des établissements d'enseignement et de recherche français ou étrangers, des laboratoires publics ou privés.

# JGR Solid Earth

## RESEARCH ARTICLE

10.1029/2022JB025216

### Key Points:

- Increasing the polydispersivity of the grain size distribution decreases the stress required for inelastic compaction
- Compaction localization is inhibited in synthetic samples with a bimodal polydisperse grain size distribution
- A transition from compaction localization to delocalized cataclasis is observed for samples with very polydisperse grain size distributions

### Supporting Information:

Supporting Information may be found in the online version of this article.

### Correspondence to:

L. Carbillet,  
[lcabillet@unistra.fr](mailto:lcabillet@unistra.fr)

### Citation:

Carbillet, L., Heap, M. J., Baud, P., Wadsworth, F. B., & Reuschlé, T. (2022). The influence of grain size distribution on mechanical compaction and compaction localization in porous rocks. *Journal of Geophysical Research: Solid Earth*, 127, e2022JB025216. <https://doi.org/10.1029/2022JB025216>

Received 19 JUL 2022  
Accepted 25 OCT 2022

### Author Contributions:

**Conceptualization:** Lucille Carbillet, Michael J. Heap, Patrick Baud, Fabian B. Wadsworth  
**Data curation:** Lucille Carbillet, Thierry Reuschlé  
**Formal analysis:** Lucille Carbillet, Michael J. Heap, Patrick Baud  
**Funding acquisition:** Michael J. Heap, Patrick Baud  
**Investigation:** Lucille Carbillet  
**Methodology:** Lucille Carbillet, Michael J. Heap, Patrick Baud, Fabian B. Wadsworth, Thierry Reuschlé  
**Project Administration:** Michael J. Heap, Patrick Baud

© 2022. The Authors.

This is an open access article under the terms of the [Creative Commons Attribution License](#), which permits use, distribution and reproduction in any medium, provided the original work is properly cited.

# The Influence of Grain Size Distribution on Mechanical Compaction and Compaction Localization in Porous Rocks

Lucille Carbillet<sup>1</sup> , Michael J. Heap<sup>1,2</sup> , Patrick Baud<sup>1</sup> , Fabian B. Wadsworth<sup>3</sup> , and Thierry Reuschlé<sup>1</sup> 

<sup>1</sup>CNRS UMR 7063, Institut Terre & Environnement de Strasbourg, Université de Strasbourg, Strasbourg, France, <sup>2</sup>Institut Universitaire de France (IUF), Paris, France, <sup>3</sup>Department of Earth Sciences, Science Labs, Durham University, Durham, UK

**Abstract** The modes of formation of clastic rocks result in a wide variety of microstructures, from poorly-sorted heterogeneous rocks to well-sorted and nominally homogeneous rocks. The mechanical behavior and failure mode of clastic rocks is known to vary with microstructural attributes such as porosity and grain size. However, the influence of the grain size distribution, in particular the degree of polydispersivity or modality of the distribution, is not yet fully understood, because it is difficult to study experimentally using natural rocks. To better understand the influence of grain size distribution on the mechanical behavior of porous rocks, we prepared suites of synthetic samples consisting of sintered glass beads with polydisperse grain size distributions. We performed hydrostatic compression experiments and found that, all else being equal, the onset of grain crushing occurs much more progressively and at lower pressure in polydisperse synthetic samples than in monodisperse samples. We conducted triaxial experiments in the regime of shear-enhanced compaction and found that the stress required to reach inelastic compaction was lower in polydisperse samples compared to monodisperse samples. Further, our microstructural observations show that compaction bands developed in monomodal polydisperse samples while delocalized cataclasis developed in bimodal polydisperse samples, where small grains were systematically crushed while largest grains remained intact. In detail, as the polydispersivity increases, microstructural deformation features appear to transition from localized to delocalized through a hybrid stage where a compaction front with diffuse bands propagates from both ends of the sample toward its center with increasing bulk strain.

**Plain Language Summary** In nature, sediments like sands and gravels in rivers, are composed of particles which can be all the same size or, more commonly, can be a mixture of lots of different sizes. Once the particles all hold together and the sediments become sedimentary rocks, the range of sizes of the particles can have an impact on how the rock behaves macroscopically under the pressure conditions of the Earth's crust. To explore this effect, we prepared synthetic rocks by sticking together particles of glass in mixture of different sizes which we then deformed under high pressure in the laboratory. Our results show that rocks made of mixture of sizes are systematically weaker than rocks with particles of a single size. Moreover, we found that, under a certain load, rocks deformed in different places in the microstructure depending on the range of sizes of the particles: in rock samples of single-size particles, the deformation is concentrated into discrete bands while the rest of the rock remain intact whereas in samples with particles of two different sizes, the deformation is distributed within the entire volume of the rock.

## 1. Introduction

The varied formation processes and source materials for clastic sedimentary rocks can produce rocks with a wide range of microstructures. For example, the grain size for clastic sedimentary rocks can vary over seven orders of magnitude, from 0.01  $\mu\text{m}$  to up to 10 cm (Guéguen & Palciauskas, 1994). The grain size of sandstones is in the range 0.06–2 mm. Although exceptionally well-sorted sandstones exist, such as the widely-studied Fontainebleau sandstone that has a broadly monodisperse grain size (Bourbie & Zinszner, 1985; Revil et al., 2014; Sulem & Ouffroukh, 2006), these are not representative of the full range of grain size distributions found for natural sandstones (Selley, 2004). Clastic rocks such as sandstones can therefore vary substantially in terms of their grain size and, importantly, grain size distribution.

Porosity is known as a first-order control on the strength of sandstones, where sandstones with high-porosity are generally weaker than those with low-porosity (Baud et al., 2014; Chang et al., 2006; Vernik et al., 1993).

**Resources:** Thierry Reuschlé  
**Software:** Thierry Reuschlé  
**Supervision:** Michael J. Heap, Patrick Baud, Fabian B. Wadsworth  
**Validation:** Lucille Carbillet  
**Writing – original draft:** Lucille Carbillet  
**Writing – review & editing:** Lucille Carbillet, Michael J. Heap, Patrick Baud, Fabian B. Wadsworth

Moreover, higher porosity favors a transition from a brittle to ductile behavior at lower pressures relative to lower porosity. Whilst high-porosity sandstones fail by shear localization (brittle regime) under relatively low pressure and by cataclastic flow (ductile regime) under high pressure, low-porosity sandstones undergo brittle faulting under a much wider range of pressures (Paterson & Wong, 2005; Scott & Nielsen, 1991; Wong et al., 1997). At stress states between the brittle faulting and cataclastic flow regimes, compaction localization was reported as a transitional failure mode in sandstones with porosity of 0.13–0.28 (Baud et al., 2004; Holcomb et al., 2007; Wong & Baud, 2012). However, to this date, no obvious link was found between the level of stress at which compaction bands nucleate and grow and the porosity of the host rock. In fact, Tembe et al. (2008) showed that this level of stress varies considerably for Bentheim, Diemelstadt and Bleurswiller sandstones, which have similar porosities. Yet, large differences in rock compositions make it difficult to unpick the effect of porosity and other microstructural attributes when studying compaction localization.

The influence of the mean grain size on the hydromechanical behavior of porous rocks has been explored in the laboratory using natural (Brace, 1961; Fredrich et al., 1990; Guyon et al., 1987; Olsson, 1974; Wasantha et al., 2015) and synthetic rocks (Carbillet et al., 2021), and using numerical modeling (Cil & Buscarnera, 2016; Ghazvinian et al., 2014; Yu et al., 2018). For porous sandstones, experimental laboratory studies using correlation analysis reported that grain size has a significant influence on uniaxial compressive strength, where the larger the grain size the lower the strength (Bell & Culshaw, 1998; Fahy & Guccione, 1979; Wasantha et al., 2015). However, other studies have also showed no significant correlation between mean grain radius and strength (Shakoor & Bonelli, 1991; Ulusay et al., 1994) and, in particular, when compared to the influence of porosity (Palchik, 1999). These conflicting findings might reflect the fact that the same mean grain size can result from very different grain size distributions and is therefore an insufficient metric for encapsulating the effect of the grain size and microstructure, especially for very heterogeneous rocks (Wasantha et al., 2015).

To analyze the relationship between the microstructural attributes, such as grain size, and the mechanical behavior of porous rocks, theoretical models have been proposed. To give an example, Zhang et al. (1990) developed an upscaled extension of the Hertzian fracture model which provides an estimate for the critical pressure for the onset of grain crushing under hydrostatic compression. They predict an inverse power law relationship between the critical pressure and the product of porosity and mean grain radius. However, since the model considers a unique value for the grain size, it does not allow for analyzing the influence of grain size distribution on the mechanical compaction of porous rocks.

The grain size distribution in a granular system can be characterized in terms of its polydispersivity and modality, which relates to sorting in detrital sedimentary rocks such as sandstones. The granular assembly is termed “monodisperse” if all particles have the same size. Any distribution of particles that deviate from the monodisperse limit is “polydisperse” to varying degrees. Specific polydisperse distributions can be monomodal, bimodal, or polymodal (Torquato, 2002). The grain size distribution has previously been identified as a control on the mechanical behavior and failure mode of lithified sedimentary rocks (Guéguen & Boutéca, 2004; Guéguen & Fortin, 2013). In particular, compaction localization is known to be promoted by microstructural homogeneity (Cheung et al., 2012; Holcomb et al., 2007; Louis, Baud, & Wong, 2007). Numerical studies also attempted to analyze the impact of grain size distribution on the strength of granular materials. For example, Wang et al. (2008) reproduced the broad phenomenology of the brittle-ductile transition using discrete element method (DEM) simulations and showed that a grain size distribution with a low polydispersivity promotes compaction localization in granular materials. However, studying the control of polydispersivity of the mechanical behavior of porous rocks in the laboratory is challenging because changes in polydispersivity are typically accompanied by variations in other microstructural parameters such as the porosity, and are intimately interlinked with attributes such as the mean pore diameter (Torquato, 2002), which also influences mechanical behavior (Xiong et al., 2021; Zhu et al., 2010). Moreover, DEM simulations are often limited to 2D and direct comparisons with experimental data are therefore fraught. To avoid variability issues presented by natural rocks, Carbillet et al. (2021) prepared synthetic sandstones using sintered glass beads, for which the porosity and grain size distribution were controlled independently. They found that, for synthetic samples with a near-monodisperse grain size distribution, increasing the mean grain radius from 112 to 601  $\mu\text{m}$  resulted in a decrease of the stress required for the onset of inelastic compaction by more than a factor of two.

The aim of this work is to study the impact of more complex grain size distributions and therefore to extend the work of Carbillet et al. (2021) by preparing and deforming samples with bimodal and monomodal (continuous)

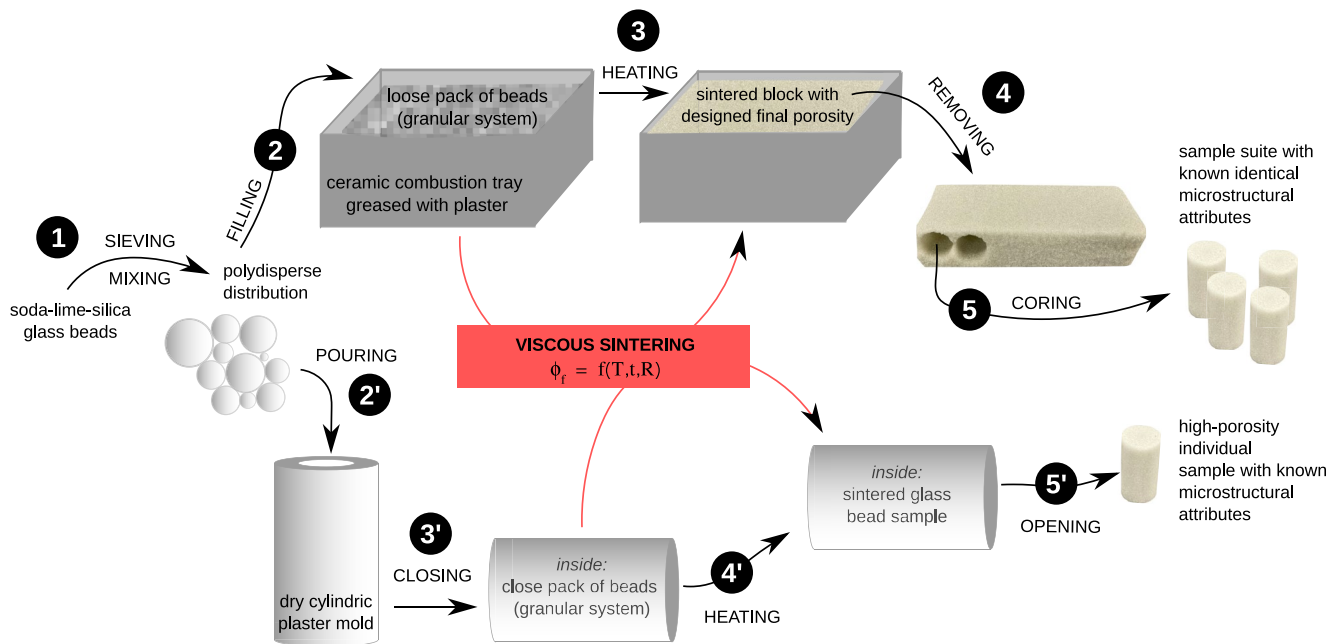


**Figure 1.** Schematics of the experimental procedure for the preparation of bidisperse and polydisperse sintered glass bead samples. Two methods were used: the preparation of suites of identical samples from sintered blocks (1–5) and the preparation of individual sintered samples (1–5′). A detailed description of each step of these two procedures is given in the main text, with references to the indices on the figure. For a given glass composition, final porosity  $\phi_f$  is a function of temperature  $T$ , time at high-temperature  $t$ , and the grain size distribution (here marked as a grain size  $R$ ).

polydisperse grain size distributions. We performed hydrostatic and triaxial compression experiments on sintered glass bead samples. The preparation procedure and sample characteristics are described in detail before we present our mechanical and microstructural results. Then we compare the results obtained on polydisperse synthetic samples with those for monodisperse synthetic samples and natural sandstones. Finally, we discuss the influence of grain size distribution on the propensity for compaction localization in porous rocks.

## 2. Materials and Methods

### 2.1. Experimental Procedure for the Preparation of the Samples

The synthetic samples used to conduct this work were prepared by the viscous sintering of spherical glass beads, following the method presented in Carbillat et al. (2021). When heated above their glass transition temperature, the beads act as liquid droplets and begin a time-dependent coalescence driven by interfacial tension, a process that progressively decreases the porosity of the system (Wadsworth et al., 2016). The rates of this process are sensitive to the polydispersity of the glass bead distributions used (Wadsworth et al., 2017).

For the purpose of this work, we prepared cylindrical synthetic samples with diameter  $\varnothing = 20$  mm and length  $L = 40$  mm starting with different grain size distributions. The experimental procedure for the preparation of the monomodal and bimodal polydisperse synthetic samples is shown in Figure 1. The distributions were designed using spherical glass beads SiLiBeads type S, in three diameter ranges: SiLiBeads #5215 (100–275  $\mu\text{m}$ ), SiLiBeads #5218 (300–710  $\mu\text{m}$ ), and SiLiBeads #4504 (900–1,400  $\mu\text{m}$ ) (the number following the # represents the company product code). Beads from these batches were first sieved into 100  $\mu\text{m}$ -diameter intervals. Monomodal and bimodal polydisperse distributions were then prepared by manually mixing known volumes of beads from the different sieved batches in a large plastic tray. These mixed batches were used to prepare synthetic samples with a porosity between 0.25 and 0.35. In the following, we detail the two techniques used for the preparation of the synthetic samples: the procedure for sintered glass beads blocks (Figure 1, steps 1–5), used to prepare samples with a porosity  $< 0.35$ , and the procedure for individual samples (Figure 1, steps 1–5′), used to prepare samples with a porosity of 0.35.

Samples with a porosity  $<0.35$  were prepared from sintered blocks, similar to the method described by Carbillet et al. (2021). To prepare sintered blocks, beads of known size distribution—designed specifically as described here above—were spooned into a ceramic combustion tray with an interior coated with a 0.5 cm-thick layer of plaster (Figure 1, step 2). The plaster layer acts as a non-stick layer and allows for the easy removal of the sintered block. To identify batch-scale inhomogeneities and prevent graded bedding from forming, the mixed beads from the plastic mixing tray were carefully spooned into the ceramic tray, while checking for homogeneity by visual inspection until the tray was full. Then, the tray was placed inside a box furnace. The bead pack was heated at a constant rate of  $3^{\circ}\text{C min}^{-1}$  to  $680^{\circ}\text{C}$  (Figure 1, step 3), which was then held constant for a certain time depending on the targeted final porosity. Halfway through the dwell period, the tray was rotated in the furnace by  $180^{\circ}$  of its initial position to reduce any heterogeneities that may arise from the temperature distribution in the furnace. At the end of the allotted sintering time, the block was cooled down to  $500^{\circ}\text{C}$  at a rate of  $1^{\circ}\text{C min}^{-1}$  and finally to ambient temperature at a rate of  $3^{\circ}\text{C min}^{-1}$ . Finally, the sintered block was removed from the tray (Figure 1, step 4). Samples with a diameter of 20 mm were cored along the horizontal axis of the block (to avoid gravitational effects) and cut and precision-ground to a nominal length of 40 mm (Figure 1, step 5).

Samples with a porosity of 0.35 were prepared individually, using single-use plaster molds to avoid damage that might result from coring samples from high-porosity sintered blocks. For each sample, a mixture of plaster and water was molded into a tube closed on one side, with external dimensions of  $\varnothing = 70$  and  $L = 90$  mm and 25 mm-thick walls. The mold was dried on a hot plate at  $50^{\circ}\text{C}$  for at least 48 hr. Then, the cylindrical mold was filled with a known distribution of glass beads (Figure 1, step 2') and a plastic cylinder with a diameter of 20 mm was used to compress the bead pack in the tube and flatten its surface. Prior to heating, the mold was closed using a  $\varnothing = 20$  and  $L = 13$  mm disk of low-porosity andesite (which is unaffected by the temperatures required for sintering, Heap et al., 2018) as an endcap to allow the mold to be cooked horizontally (Figure 1, step 3'). This allowed us to prevent gravity forces from generating a porosity gradient in the axial direction of the cylindrical sample (see Wadsworth et al., 2016 for a discussion of the effect of compaction gradients for tall samples/systems). The assembly was sintered at  $680^{\circ}\text{C}$  (Figure 1, step 4'), using the same workflow used for the sintered blocks. Once the temperature in the furnace had been reduced to room-temperature, the plaster mold was taken out of the furnace and the sintered sample was retrieved (Figure 1, step 5') by gently breaking the plaster mold using a hammer. Although the individual sample method allows for a complete control over the grain size distribution, it could only be used to prepare high-porosity samples (0.35) because the sample cylindrical geometry is only preserved at incipient stages of sintering and would slump and change if allowed to sinter further.

Here we do not dwell on (or report) the specific times that each sample was sintered for at high temperature. However, we note that in general, for a given bead size distribution, longer sintering times will be represented as lower sample porosities, and samples comprising smaller grains will also sinter more rapidly to lower porosities. The purpose here is simply to output samples of a range of porosities in such a way that we can reliably reproduce the procedure. The reader is referred to Wadsworth et al. (2016) for overviews of the kinetics involved for the purposes of experimental design.

## 2.2. Description of the Samples

The sample dimensions,  $\varnothing$  and  $L$ , and mass  $m$  were measured and the total porosity  $\varphi$  calculated using  $\varphi = 1 - [m/(\rho_s V_b)]$ , where the sample bulk cylindrical volume is  $V_b = \pi R^2 L$ , with  $R = \varnothing/2$ , and  $\rho_s$  the glass solid density, which is the same before and after heating to  $680^{\circ}\text{C}$  and equal to  $2.49 \text{ g cm}^{-3}$ . The total porosity of the samples used in this study is between 0.25 and 0.35, with an average uncertainty of  $\pm 0.005$ . The microstructural attributes of the synthetic samples are presented in Table 1. In total, eight different bead size distributions, presented graphically in Figure 2, were used to prepare synthetic samples. For each distribution, the first  $M_1$ , second  $M_2$ , and third  $M_3$  moments were calculated (using Equation S1 as described in the Supporting Information S1) and the degree of polydispersity  $S$  was calculated using  $S = M_1 M_2 / M_3$  (Torquato, 2002; Wadsworth et al., 2021).  $S$  is in the range 0–1, where 0 is highly polydisperse and 1 is the monodisperse limit.

The degree of polydispersity of the distributions varies between 0.60 and 0.89. In addition, the distributions can be segregated into two categories, depending on type of grain size distribution: bimodal polydisperse (BP) distributions correspond to samples with two different sizes of grains and monomodal polydisperse (PP) distributions to those with a continuous variation of grain size with one monomodal peak. In the following, the bimodal and monomodal polydisperse distributions will be referred to simply as “bidisperse” and “polydisperse” for simplicity

**Table 1**  
*Microstructural Attributes of the Synthetic Samples and Critical Stress Values for the Onset of Inelastic Compaction Under Triaxial Conditions ( $C^*$ ) and Hydrostatic Conditions ( $P^*$ )*

Sample	Porosity $\varphi$ $\pm 0.005$	Polydispersivity $S$ (0: polydisperse limit; 1: monodisperse limit)	Mean grain diameter $D_m$ ( $\mu\text{m}$ )	Confining pressure $P_c$ (MPa) ( $P_p = 10$ MPa)	Critical stress $C^*$	
					Differential stress $Q$ (MPa)	Effective mean stress $P$ (MPa)
PP8915	0.297	0.89	454	70	67	72
PP8914	0.301			90	61	90
PP8913	0.290			110	47	106
PP8912	0.297			130	30	120
PP8911	0.291			Hydrostatic loading	$P^*$	
					0	136
PP8916	0.303			Hydrostatic loading	$P^*$	
					0	139
PP6414	0.256	0.64	456	50	76	55
PP649	0.252			80	83	88
PP6410	0.249			110	77	116
PP641	0.251			140	70	133
PP643	0.257			170	46	165
PP642	0.253			Hydrostatic loading	$P^*$	
					0	170
BPA5521	0.361	0.78 (bidisperse)	862	Hydrostatic loading	$P^*$	
					0	47
BPA5531	0.360			Hydrostatic loading	$P^*$	
					0	48
BPA7361	0.357	0.71 (bidisperse)	726	Hydrostatic loading	$P^*$	
					0	27
BPB5541	0.351	0.60 (bidisperse)	712	Hydrostatic loading	$P^*$	
					0	27
BPC3742	0.354	0.83 (bidisperse)	434	35	12	20
BPC3744	0.357			Hydrostatic loading	$P^*$	
					0	53
BPC5543	0.350	0.76 (bidisperse)	374	35	15	30
BPC5546	0.352			Hydrostatic loading	$P^*$	
					0	45
BPC7321	0.360	0.70	314	25	12	17
BPC7322	0.361			Hydrostatic loading	$P^*$	
					0	31

(while noting that the bimodal polydisperse distributions are not strictly bidisperse). Figure 2 includes small schematics that represent bimodal and monomodal polydisperse distributions, which will be repeated in the figures presented throughout this manuscript to facilitate comprehension.

For the purpose of the study, two polydisperse distributions (Figures 2a and 2b) and six bidisperse distributions were prepared (Figures 2c–2h). The polydisperse distributions (a) PP89 and (b) PP64 have a similar mean grain diameter, approximately  $D_m = 455 \mu\text{m}$ , but the latter is less closely clustered, that is, more polydisperse with a



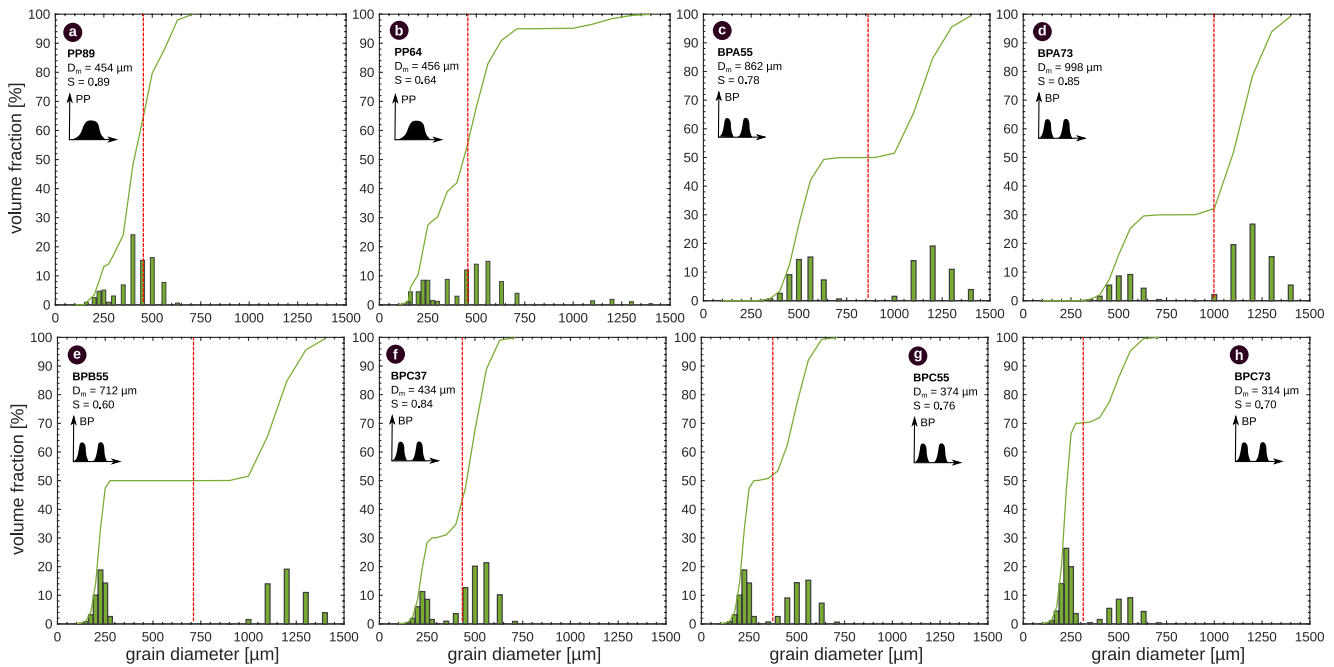


**Figure 2.** Grain size distributions of the synthetic samples. The distributions are presented in terms of volume fraction against grain diameter, with the cumulative volume fraction (green solid lines) and the first moment of the distribution  $M_1$ , that is, the mean grain diameter (here termed  $D_m$ ; dashed red lines). Distributions (a) PP89 and (b) PP64 are monomodal polydisperse distributions, and distributions (c) BPA55, (d) BPA73, (e) BPB55, (f) BPC37, (g) BPC55 and (h) BPC73 are bimodal polydisperse distributions. The mean grain diameter  $D_m$  and the degree of polydispersity  $S$  of each distribution are given on the corresponding plot, above a schematic which indicates qualitatively the distribution type (monomodal polydisperse, PP, or bimodal polydisperse, BP). For clarity, these schematics will be used throughout the manuscript.  $S$  is in the range 0–1, where 1 is the monodisperse limit.

lower  $S$ . The bidisperse distributions have different volume fractions of grains with diameters of 224 (refer to as small beads), 523 (medium beads), and 1,203  $\mu\text{m}$  (large beads).

Although it does not accurately capture the size of the grains that compose the bidisperse samples, the mean grain diameters of the bidisperse distributions are also indicated in Figure 2 (dashed red lines). For simplicity, the naming system used to differentiate between the bidisperse distributions is presented in a table in Supporting Information S1. Overall, the samples composed of the largest grains are those prepared using the BPA distributions, and those with the smallest grains are those prepared using the BPC distributions (Figure 2).

Backscattered scanning electron microscope (SEM) images of synthetic samples with polydisperse and bidisperse grain size distributions are presented in Figure 3. As predicted theoretically by viscous sintering theory (Frenkel, 1945; Mackenzie & Shuttleworth, 1949; Wadsworth et al., 2016), the width of the necks found at grain-to-grain contacts increases progressively, from a point-contact geometry at high porosity close to the initial packing state of the beads, to a wide neck with no remnant interface visible at lower relative porosities (compare Figure 3a with Figure 3b). Similar to the monodisperse synthetic samples prepared previously (Carbillet et al., 2021), microscopic heterogeneities can be observed in the samples prepared herein, especially in the samples with the highest porosity values (Figures 3c and 3d). However, 2D porosity measurements performed by image analysis on the micrographs (using a square window of 2 mm of edge-length in ImageJ), yield closely clustered monomodal distributions. As random variations in the microstructure occur on length scales much smaller than the sample lengths, the synthetic samples prepared are statistically homogeneous at the sample scale.

### 2.3. Deformation Experiments

For the purpose of this study, we performed two types of deformation experiments: hydrostatic and triaxial compression experiments. All the experiments were performed under saturated and drained conditions using the triaxial press at the Strasbourg Institute of Earth & Environment (France).

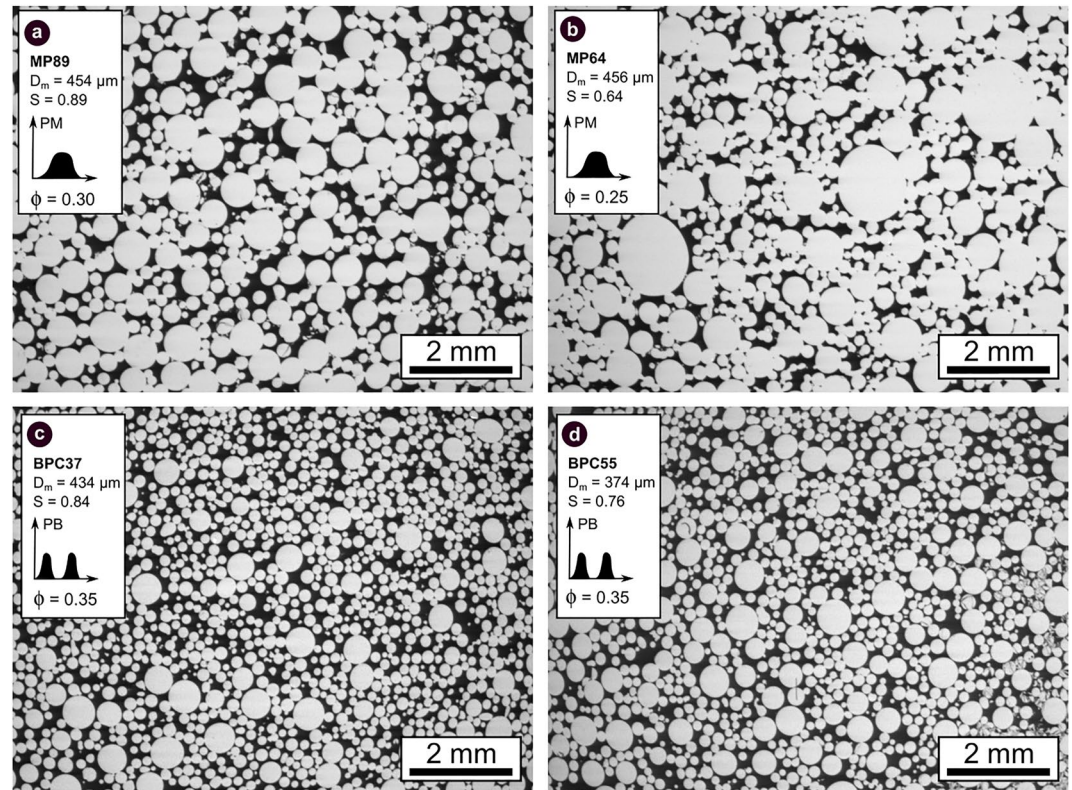


**Figure 3.** Microstructure of intact samples with a polydisperse grain size distribution (a) PP89 and porosity of 0.30 and (b) PP64 and porosity of 0.25 and a bidisperse grain size distribution (c) BPC37 and porosity of 0.35 and (d) BPC55 and porosity of 0.35. The degree of polydispersity  $S$  is in the range 0–1, where 1 is the monodisperse limit.

Prior to testing, all the synthetic samples were dried in a vacuum oven at 40°C for at least 48 hr. The samples were then jacketed with thin (<1 mm-thick) copper foil and vacuum-saturated with de-aired, deionized water. Samples were then placed between two steel endcaps within a Viton jacket, to ensure the separation between the pore fluid and confining fluid, and mounted in the pressure vessel. The triaxial apparatus contains three servo-controlled independent circuits: a confining pressure  $P_c$  circuit (kerosene), a pore pressure  $P_p$  circuit (deionized water), and an axial pressure circuit, the latter of which provides the axial load by moving an axial steel piston.

During the tests, the applied axial force was measured using a pressure probe in the axial pressure circuit, and the axial displacement of the piston was measured using a linear variable differential transformer (LVDT). Using the initial dimensions of the sample, axial stress and strain were calculated from these values. Porosity change was also calculated from the conversion of pore volume change given by the displacement of the piston in the pore pressure intensifier. Finally, acoustic emissions (AEs) were recorded using a USB AE Node from Physical Acoustics and a piezoelectric transducer (with a frequency bandwidth of 200–900 kHz) attached to the piston. The software AEWIn, with a detection threshold for an AE hit set at 28 dB, was used to monitor the AEs energy, that is, the area under each received AE waveform.

We used the same experimental procedure described in Carbillat et al. (2021) to perform hydrostatic and triaxial experiments. We assume a simple effective pressure law  $P_{\text{eff}} = P_c - P_p$  and adopt the convention that compressive stress and compactive strain are positive. All experiments, hydrostatic and triaxial, were performed using a constant pore pressure  $P_p$  of 10 MPa.

During hydrostatic compression, the effective pressure  $P_{\text{eff}}$  was increased in steps (corresponding to an average rate of  $10^{-4}$  MPa  $s^{-1}$ ) until the pressure required for the onset of grain crushing  $P^*$  was reached (Zhang et al., 1990). Pressure steps were varied between 1 and 10 MPa depending on the time necessary to reach equilibrium at the previous step, which we assumed to be achieved when the pore volume changed at a rate lower than  $10^{-2}$   $s^{-1}$ . Triaxial compression was achieved by superposing an axial pressure to a hydrostatic pressure. First,



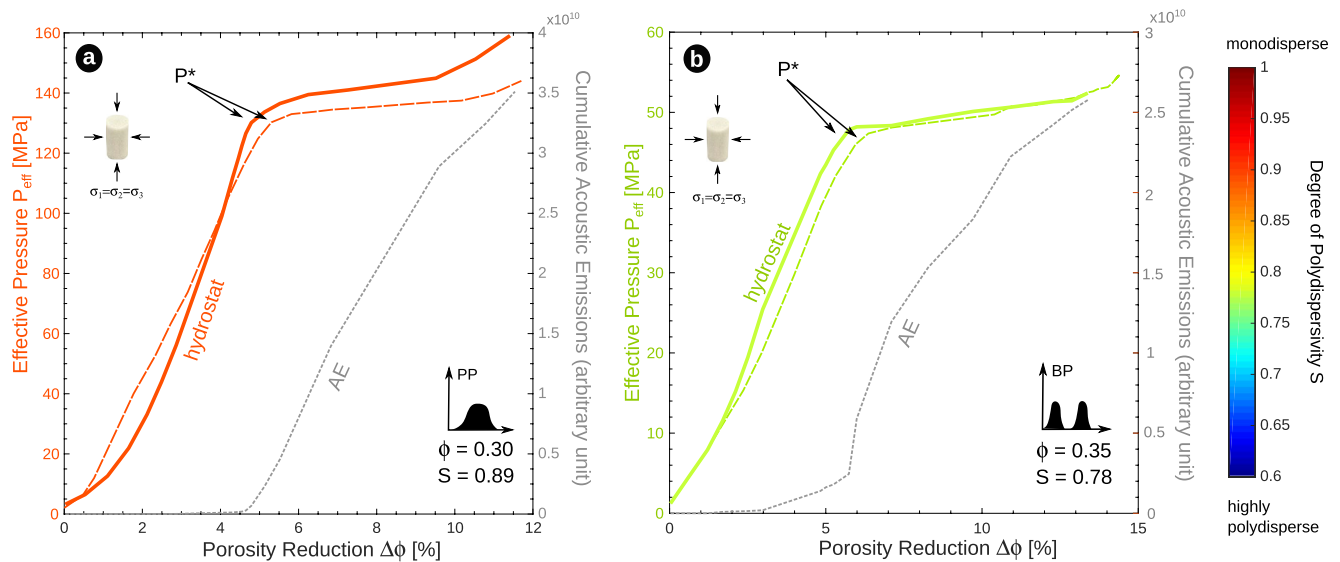


**Figure 4.** Mechanical data (colored lines) and acoustic emission (AE) energy (gray lines) for the hydrostatic compression of (a) polydisperse synthetic samples PP8911 (dashed red line) and PP8916 (bold red line) and (b) bidisperse synthetic samples BPA5521 (dashed green line) and BPA5531 (bold green line). To demonstrate reproducibility, each panel shows the data for two experiments performed on samples with identical microstructural attributes.

the sample was placed under hydrostatic conditions by increasing  $P_{\text{eff}}$  to a target value, with  $P_p = 10$  MPa, and the system was left to equilibrate overnight. Then, an axial force was applied by advancing the loading piston on top of the sample at a servocontrolled rate corresponding to a strain rate of  $10^{-5} \text{ s}^{-1}$ . The difference between the axial stress ( $\sigma_1$ ) and the confining pressure ( $\sigma_3$ ) is referred to as differential stress  $Q$  (i.e.,  $Q = \sigma_1 - \sigma_3$ ). The effective mean stress  $P$  was calculated for both hydrostatic and triaxial experiments as the difference between the mean stress and the pore pressure, that is,  $P = (\sigma_1 + 2\sigma_3) / 3 - P_p$ . All triaxial tests were performed in the ductile regime and samples were deformed up to axial strain considered suitable for subsequent microstructural observations using the SEM, that is, 4% if the mechanical data showed stress drops (as a result of compaction localization; Baud et al., 2004) and 6% if not. Unloading was also performed at  $10^{-5} \text{ s}^{-1}$  and the pore and confining pressures were removed slowly to preserve the deformed samples. Polished thin sections for microstructural inspection using an SEM were prepared using selected post-deformation samples.

### 3. Results: Hydrostatic Compression

#### 3.1. Mechanical Data and Microstructural Observations

Examples of the mechanical and AE data for hydrostatic compression experiments performed on the samples with a polydisperse and bidisperse grain size distribution are shown in Figures 4a and 4b, respectively. We first note that the experiments are reproducible between samples with identical microstructural attributes (Figure 4). The results for polydisperse and bidisperse samples are qualitatively similar and show four phenomenological stages. First, the porosity decreases non-linearly as  $P_{\text{eff}}$  is increased and no AEs are recorded. Then, the porosity decreases broadly linearly with increasing  $P_{\text{eff}}$  whilst the AE activity remains low. When  $P_{\text{eff}}$  reaches a threshold value, the critical pressure for grain crushing  $P^*$  (Zhang et al., 1990), AE activity suddenly increases and, concomitantly, the slope of the mechanical data decreases. The values for  $P^*$  are compiled in Table 1. Beyond  $P^*$ , the porosity decreases substantially as  $P_{\text{eff}}$  is increased (porosity decreases by up to 6% for a 10 MPa increase in  $P_{\text{eff}}$ ) and the samples undergo a bit of hardening (Figure 4).

The microstructures of a polydisperse sample and a bidisperse sample deformed under hydrostatic compression to beyond  $P^*$  are presented in Figure 5. The SEM images show that the substantial porosity reduction beyond  $P^*$  is due to extensive distributed grain crushing, which affects all grains, whatever their size, and despite the differences in initial porosity and polydispersivity. Further, no differences were observed between the polydisperse and the bidisperse synthetic samples in terms of the microstructural features that develop under hydrostatic compression (Figure 5).

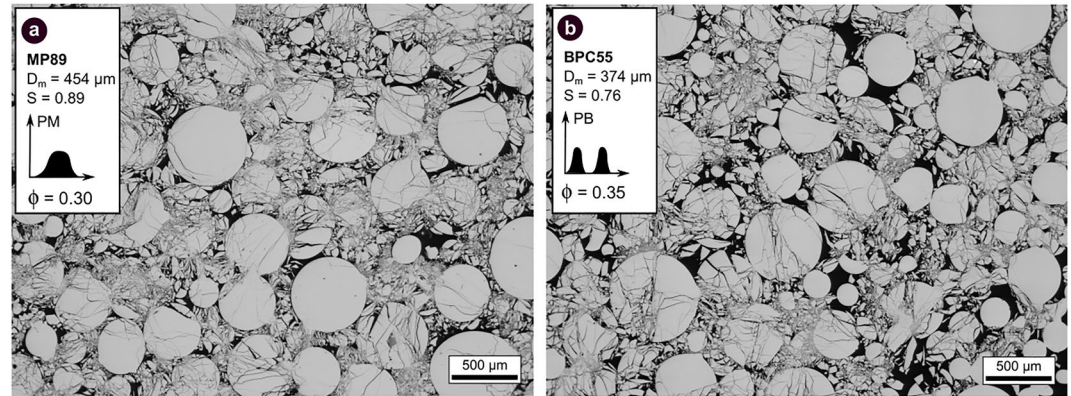


**Figure 5.** Representative backscattered scanning electron microscope images showing the microstructure of synthetic samples deformed under hydrostatic loading up to an effective stress beyond  $P^*$  for (a) a polydisperse grain size distribution and porosity of 0.30 and (b) a bidisperse distribution and a porosity of 0.35. Extensive grain crushing is observed for both types of distributions. Black: porosity, gray: glass.

### 3.2. Influence of Polydispersity

The bidisperse samples deformed under hydrostatic compression, which have a porosity of approximately 0.35, span a large range of polydispersity (0.60–0.83). Figure 6 presents the results of the hydrostatic tests conducted on the bidisperse samples. Overall, our mechanical data show that changing the polydispersity  $S$  from 0.60 to 0.83 (i.e., toward a more monodisperse distribution) increases the pressure required for the onset of grain crushing  $P^*$  from 27 to 57 MPa (Figure 6). Figure 6b shows that the evolution of  $P^*$  with  $S$  is well described by a positive linear slope over the range of polydispersity investigated. Therefore, our results suggest that the higher the polydispersity of the grain size distribution (i.e., the lower the value of  $S$ ), the lower the stress required for the onset of grain crushing.

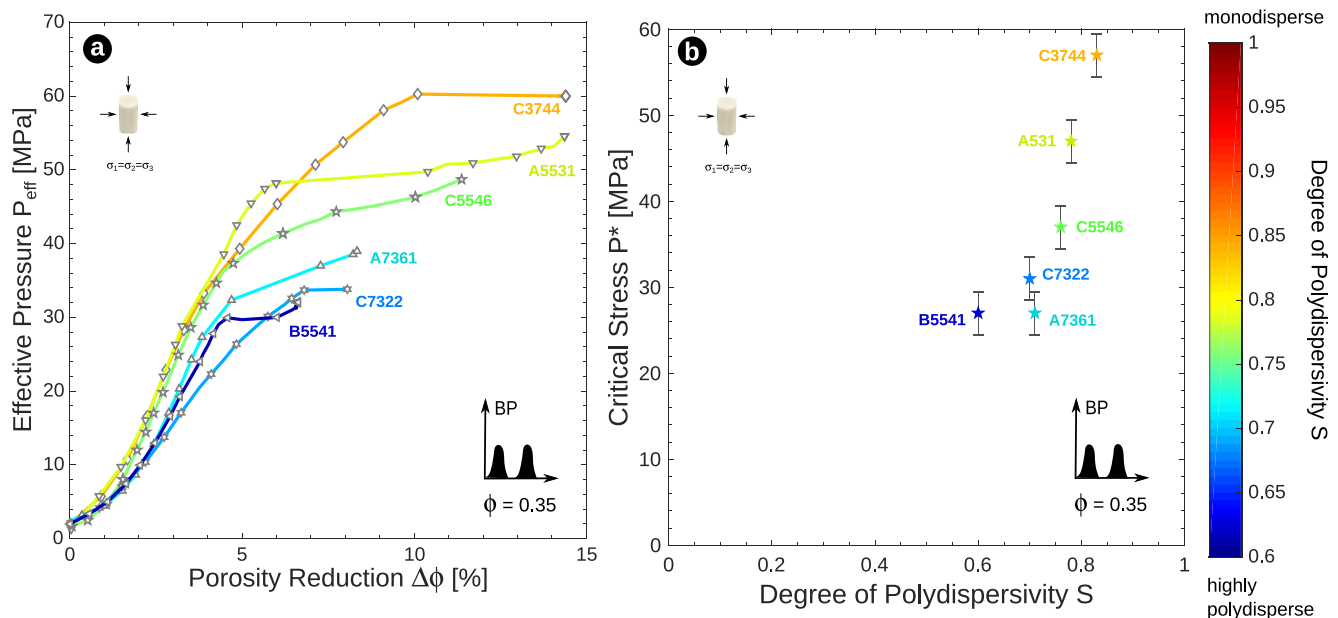


**Figure 6.** Mechanical data for the hydrostatic compression of bidisperse synthetic samples with a porosity of 0.35. (a) The hydrostatic curves are shown as the effective pressure against the porosity reduction, using a colormap for the degree of grain size distribution polydispersity. The name of the grain size distribution of each sample is indicated at the end of the corresponding hydrostat and corresponds to both Table 1 and Figure 2. (b) The critical stresses for the onset of grain crushing ( $P^*$ ) are plotted against polydispersity.

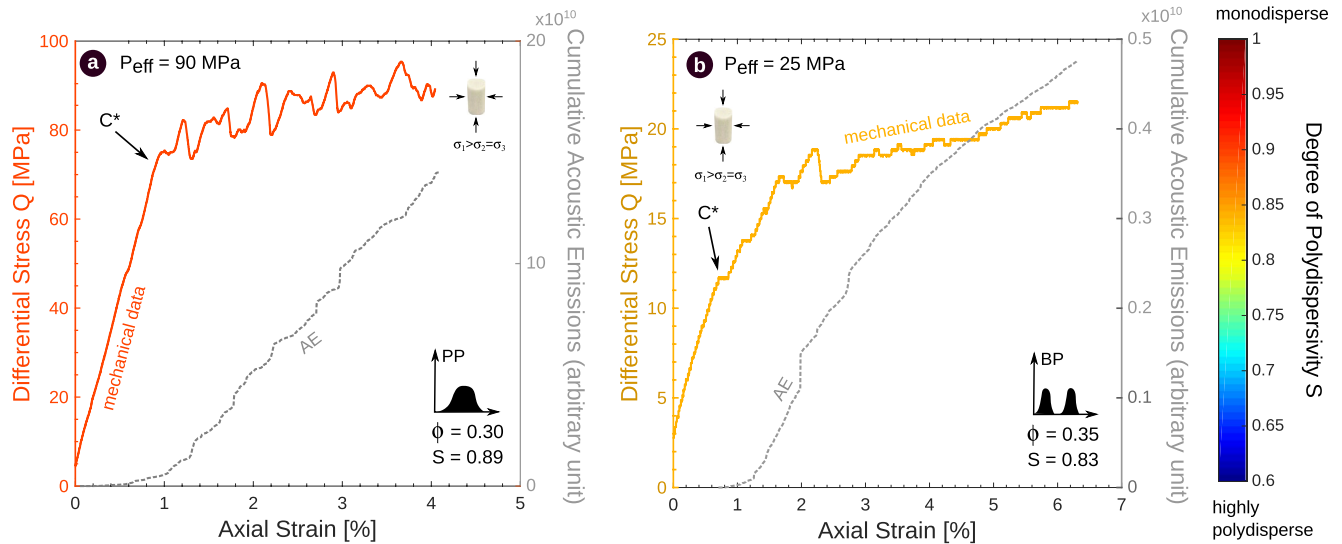


**Figure 7.** Mechanical data (solid lines) and cumulative acoustic emission energy (dashed gray lines) for triaxial tests performed on (a) a polydisperse synthetic sample PP8914 and (b) a bidisperse synthetic sample BPC3742 in the ductile regime.

## 4. Results: Triaxial Compression

### 4.1. Mechanical Data

An example of the mechanical (solid colored lines) and AE (dashed gray lines) data for triaxial deformation experiments performed on samples with a polydisperse and bidisperse grain size distribution is shown in Figures 7a and 7b, respectively. Qualitatively speaking, the data show a first stage where the axial strain increases linearly with  $Q$  and where the AE activity is low. In a second stage, the slope of the stress-strain curves deviates from linearity and there is an acceleration in AE activity, marking the transition to the inelastic regime of deformation. The critical stress for inelastic deformation, the onset of shear-enhanced compaction, is termed  $C^*$  (labeled on Figure 7). The values for  $C^*$  for all experiments are compiled in Table 1. Beyond  $C^*$ , the mechanical data for polydisperse and bidisperse samples deformed in the ductile regime are different: the stress-strain curves for polydisperse samples show numerous stress drops, concomitant with small bursts in AE activity, whilst the stress-strain curves for bidisperse samples show far fewer, and less pronounced, stress drops (Figure 7).

The complete mechanical data set for polydisperse samples and bidisperse samples are shown in Figures 8 and 9, respectively. The effective mean stress-porosity reduction curves for triaxial tests are compiled with the corresponding curve for hydrostatic pressurization. When plotted in the differential stress-effective mean stress space, the values for the stress required to reach  $C^*$  and  $P^*$  map out compactive yield caps for the two polydisperse grain size distributions investigated. The yield caps for our polydisperse samples have an elliptical shape (Figures 8c and 8d). In detail, the polydisperse samples with a porosity of 0.25 have a higher compactive yield stress values than those with a porosity of 0.30 (Figures 8a and 8b). As a result, the compactive yield cap for the polydisperse samples with a porosity of 0.25 is comparatively larger than that with a porosity of 0.30 (Figures 8c and 8d).

When comparing the mechanical data sets for polydisperse and bidisperse samples, we notice more, and larger, stress drops in the mechanical data for the polydisperse samples than in those for the bidisperse samples (Figures 7–9). These stress drops, and the concomitant surges in AE activity, are mechanical instabilities that often result from the occurrence of compaction localization (Baud et al., 2004). In the following, to further interpret our mechanical data, we present microstructural observations made on the polydisperse and bidisperse samples post-deformation.

### 4.2. Microstructural Observations

The deformation features observed in polydisperse and bidisperse samples deformed in the ductile regime are presented in Figures 10 and 11, respectively. In the polydisperse samples, mechanical compaction was found to

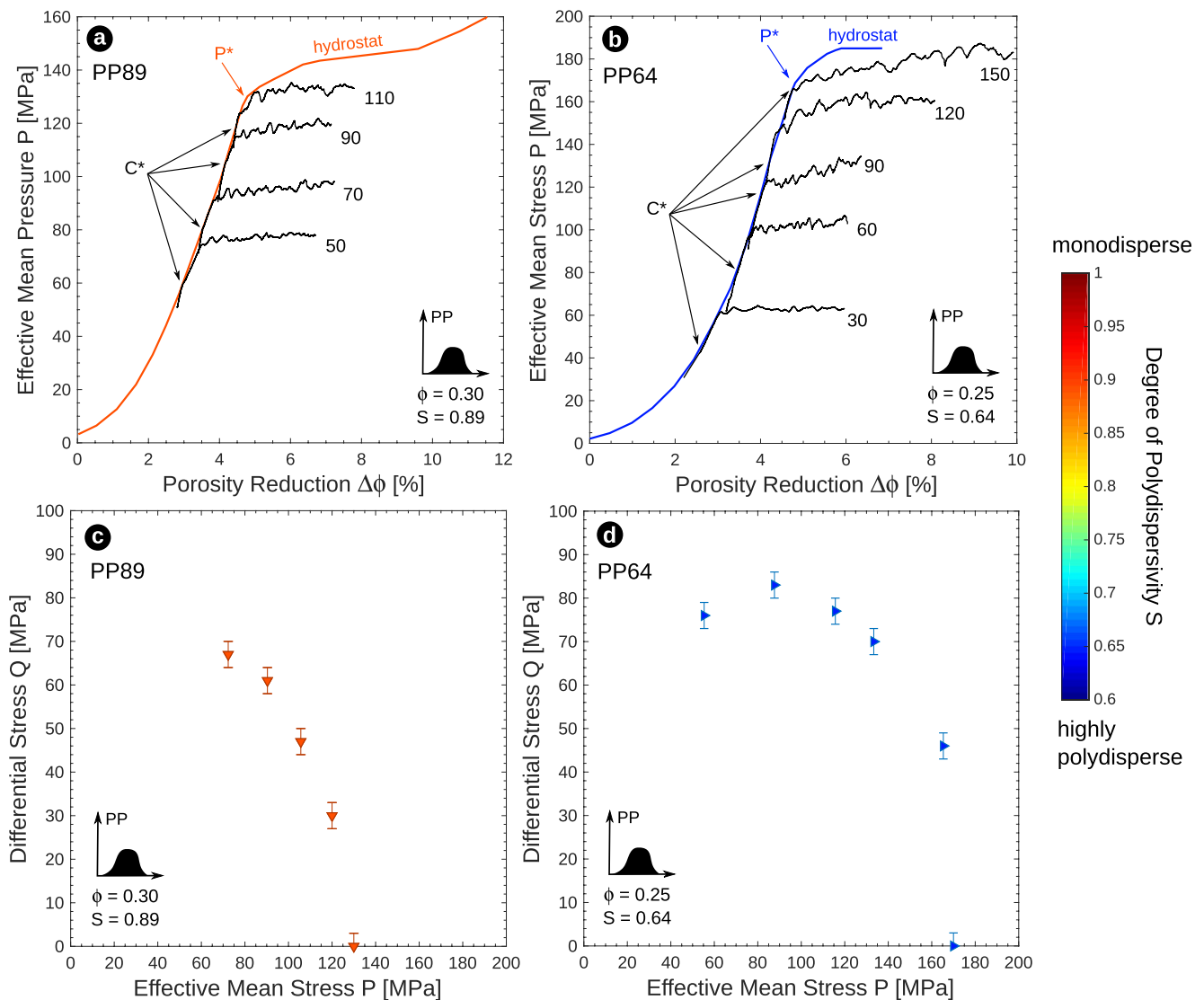


**Figure 8.** Hydrostatic and triaxial mechanical data for polydisperse (PP) synthetic samples. The effective mean stress–porosity reduction curves for triaxial tests (black lines) are compiled with the corresponding hydrostatic curve (colored lines) for samples with a grain size distribution PP89 (a) and PP64 (b). The effective pressures applied during the triaxial tests are indicated at the end of each corresponding curve. The critical stress values ( $C^*$  and  $P^*$  compiled in Table 1) are plotted in the  $P$ – $Q$  stress space where they map out the compactive yield caps for the distributions (c) PP89 and (d) PP64.

form a front growing from both ends of the samples and advancing toward the center with increasing axial strain (Figures 10a and 10c). For the polydisperse sample with a higher relative value of  $S$  (i.e., closer to monodisperse), 200–500  $\mu\text{m}$ -thick compaction bands were observed in the deformed zones, close to the boundary between the largely intact material and the deformation front (Figure 10b). This observation suggests that mechanical compaction took place by growth of compaction bands perpendicular to the maximum principal stress from the ends of the sample first, and then progressively toward the center. For the polydisperse sample with a lower value of  $S$  (0.64), that is, the more disperse sample, the presence of compaction bands in the deformed zones is more ambiguous. However, very tortuous bands of crushed beads appear to have formed without pervasively crushing of largest grains (Figures 10d and 10e). In the bidisperse samples, delocalized cataclasis was observed (Figure 11). Regardless of the relative percentage of large grains compared to small grains, our microstructural observations reveal that the larger grains remained intact but that the smaller grains were extensively crushed. This observation is in agreement with our mechanical data, where the stress–strain curves for the bidisperse samples show almost no stress drops (Figure 7).



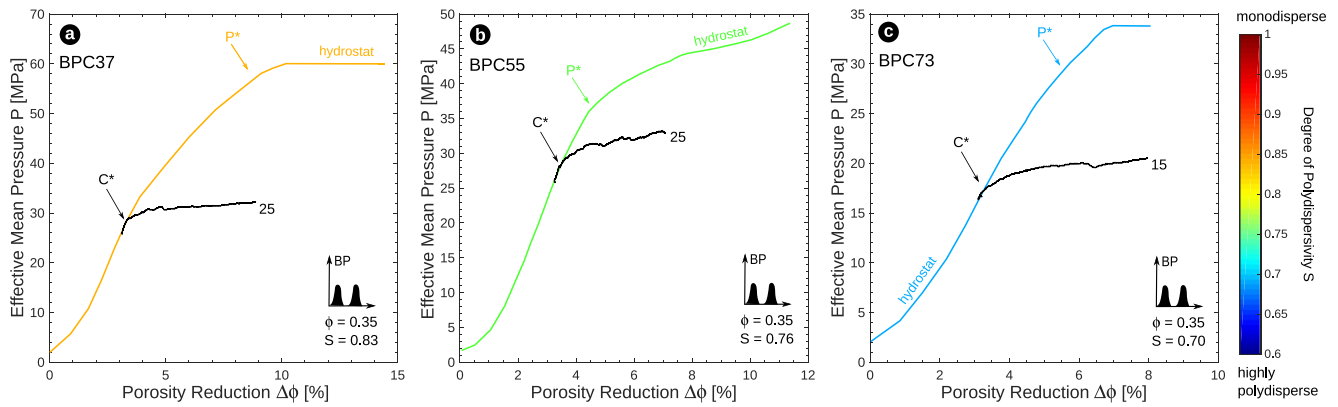


**Figure 9.** Hydrostatic (colored lines) and triaxial mechanical data (black lines) presented as the effective mean stress against the porosity reduction for bidisperse (BP) synthetic samples with a grain size distribution (a) C37, (b) C55, and (c) C73. The effective pressures applied during the triaxial tests are indicated at the end of each corresponding curve.

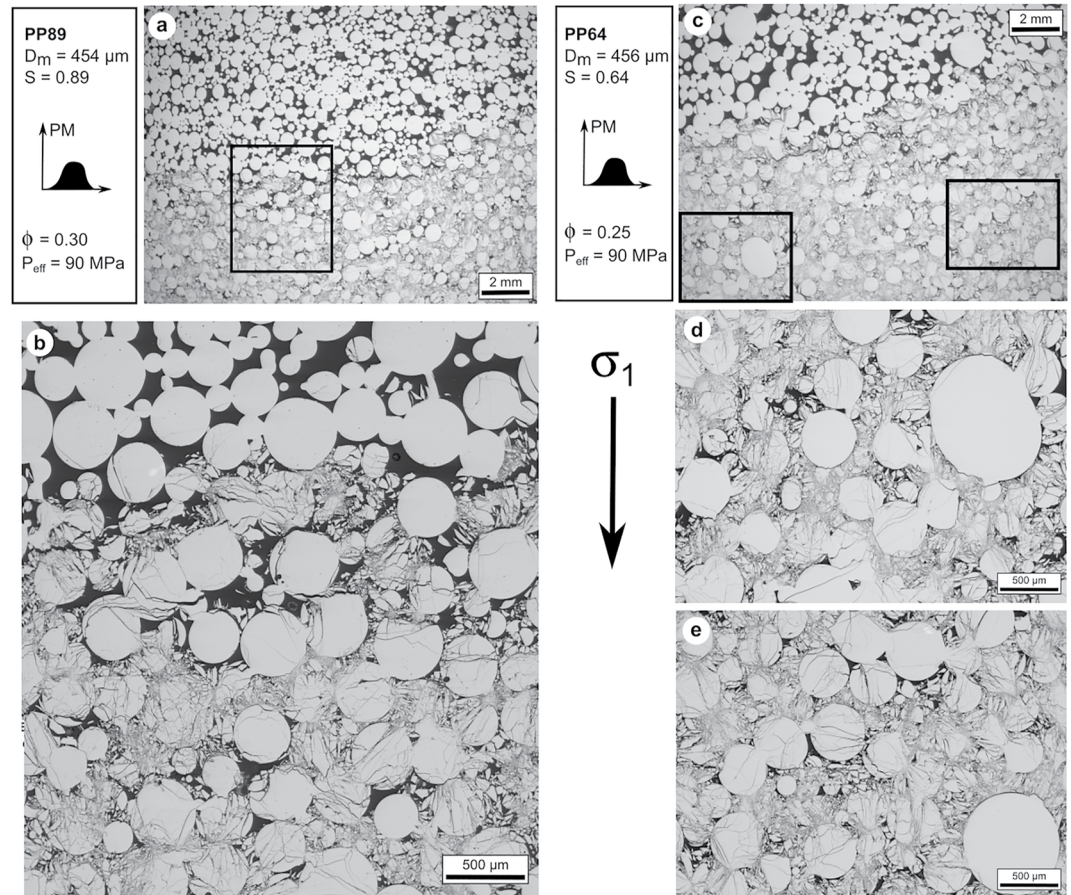


**Figure 10.** Representative backscattered scanning electron microscope images of the microstructure of polydisperse synthetic samples deformed under triaxial compression up to stresses beyond  $C^*$ . At a degree of polydispersity  $S = 0.89$  and porosity of 0.30 (a), mechanical compaction features spread from the ends toward the center of the sample and form (b) compaction bands. At a degree of polydispersity of  $S = 0.64$  and a porosity of 0.25, (c) mechanical compaction spread from the extremities toward the center of the sample, (d, e) without affecting the bigger grains. Black: porosity, gray: glass.



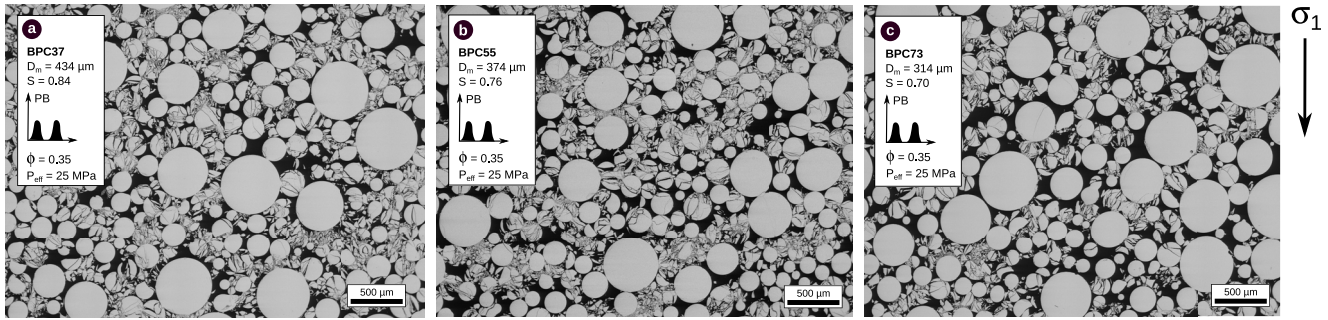


**Figure 11.** Representative backscattered scanning electron microscope images of the microstructure of bidisperse synthetic samples deformed under triaxial compression up to stresses beyond  $C^*$ . From (a–c), the ratio of small grains to big grains decreases. For all distributions, distributed compaction, where small grains are crushed while bigger grains remain intact, is observed. Black: porosity, gray: glass.

## 5. Discussion

### 5.1. Comparison Between Polydisperse and Monodisperse Sintered Glass Beads Samples

The deformation of sintered glass bead samples with monodisperse grain size distributions and different mean grain diameters have been studied by Carbillet et al. (2021). In the following, we compare the results reported in Carbillet et al. (2021) with those collected for bidisperse and polydisperse synthetic samples in this study. Figure 12 shows a comparison of mechanical data obtained on monodisperse, bidisperse, and polydisperse samples under hydrostatic and triaxial compression. When submitted to hydrostatic loading, bidisperse and monodisperse synthetic samples behave differently in two main aspects: (a) at constant porosity, the stress required to reach  $P^*$  is higher for a sample with a monodisperse distribution than for all samples with a bidisperse distribution, whatever the polydispersivity; (b) while the transition to inelastic deformation at  $P^*$  is associated with a sharp increase in the reduction of porosity for the monodisperse sample, this transition is more progressive for the bidisperse samples. The difference in the stress required to reach  $P^*$  might be partly due to a difference in the mean or characteristic grain size, which was found to be negatively correlated to the stress required for the onset of inelastic compaction (Carbillet et al., 2021). In Figure 12a, the mean grain diameter of the monodisperse sample is 224  $\mu\text{m}$  whereas the mean grain diameters of the bidisperse samples are in the range 314–998  $\mu\text{m}$ . Moreover, complexities might arise from the fact that our bidisperse synthetic samples are prepared with variable

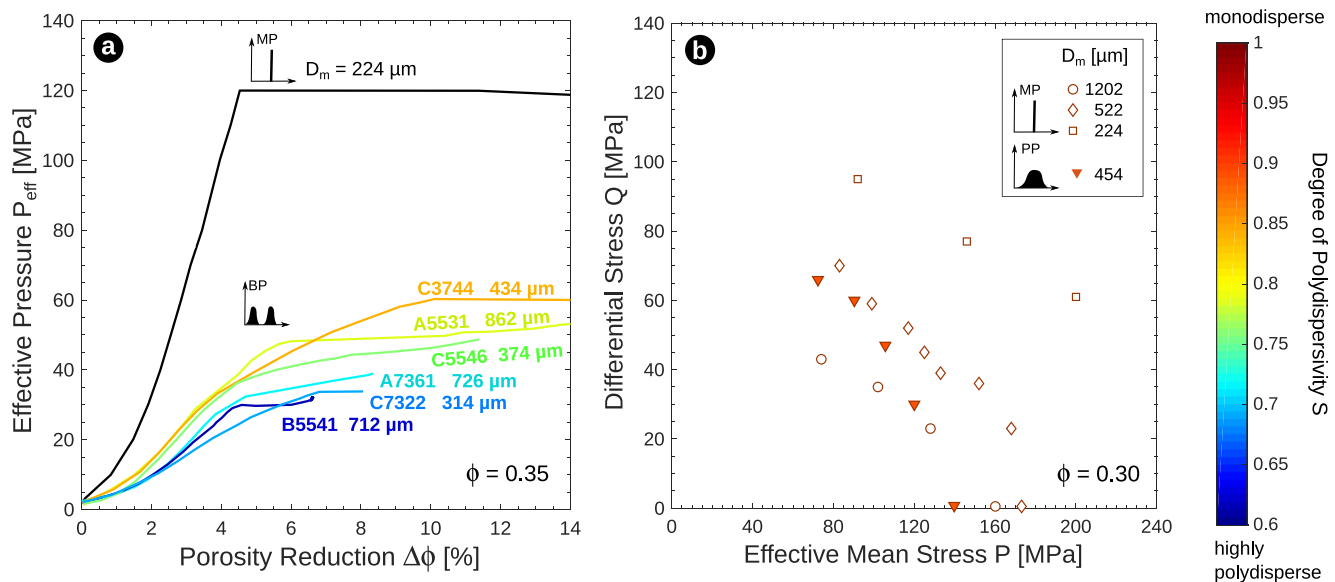


**Figure 12.** (a) Hydrostatic curves for synthetic samples with a porosity of 0.35 and with bidisperse (BP, colored curves) and monodisperse (MP, black curve) grain size distributions. (b) Compactive yield caps of synthetic samples with a porosity of 0.30 and polydisperse (PP, solid triangles) and monodisperse (open symbols) grain size distributions. The mean of the grain size distributions is given as  $D_m$  and the degree of polydispersivity  $S$  is color coded using the color scale on the right.

proportions of large, medium, and small beads (Figure 2 and Table S2 in Supporting Information S1). Therefore, the differences in strength due to changes in the grain size are integrated with those due to changes in the polydispersivity of the grain size distribution. For instance, we note that  $P^*$  is slightly higher for the distribution BPC73 than for BPA73 although the latter is less polydisperse and therefore expected to be lower. The difference in  $P^*$  might be explained by the fact that the distribution BPA73 contains 70 vol% of large beads and 30 vol% of medium beads while the distributions BPC73 contains no large beads but 70 and 30 vol% of medium and small beads, respectively. However, over the ranges of grain size and polydispersivity investigated, our data suggest that the degree of polydispersivity has a stronger control over  $P^*$  than the mean grain size for bidisperse samples. Moreover, although differences in the relative proportion of large grains to small grains might explain some of the difference in  $P^*$ , it is not sufficient to explain the very low  $P^*$  values found for the bidisperse samples compared to monodisperse samples.

When comparing the compactive yield cap for polydisperse samples with those for monodisperse samples we observe that, for a same porosity and similar mean grain diameter, the stresses required to reach  $C^*$  are lower for the polydisperse synthetic samples (Figure 12b). This observation concurs with the result that samples with a very disperse grain size distribution undergo inelastic compaction at lower stress states than those with a more closely clustered distribution, closer to the monodisperse limit. When we consider the results for monodisperse samples only, it appears that a much larger reduction in stress results from the increase in mean grain diameter. Therefore, according to the compilation in Figure 12b, the mean grain size appears to exert a higher-order control on the critical stress for the onset of shear-enhanced compaction than the degree of polydispersivity. However, this observation is limited to the ranges of grain size and polydispersivity investigated in the present study, which are much smaller than those observed in natural porous rocks (Carbillet et al., 2021).

Under an externally applied stress, the bulk mechanical response of granular rocks is controlled by the arrangement of forces at the grain-scale, that is, by the morphology of the force chain network, defined as the subset of grain-to-grain contacts carrying the largest forces in the system (Guéguen & Boutéca, 2004). Indeed, mechanical deformation is predicted to occur in the strong force network, which carries a force larger than the average force in the system (Zhang et al., 2017). Moreover, discrete element simulations suggest that the strong network only involves a selected number of grains within the microstructure (Peters et al., 2005; Vallejo et al., 2005). To probe the influence of the grain size distribution of granular materials on the geometry and distribution of the force chains, diverse methods of numerical modeling have been developed over the past decades (Papadopoulos et al., 2018). In this study, the mechanical data obtained using simplified two-phases granular samples suggest that increasing the polydispersivity of the grain size distribution decreases the stress required to reach inelastic compaction. This is in agreement with the results from both Lan et al. (2010) and Peng et al. (2017) who reported that numerical samples with a more monodisperse grain size distribution fail at higher stress under uniaxial compression. However, Muthuswamy and Tordesillas (2006) also found that straight force chains with a higher degree of branching, which results in a macroscopically stronger granular material, are more likely to form in more polydisperse samples, which in their case also have a lower average packing density. In detail, the microstructural data show that deformation affects the small grains more than the large grains, suggesting that force chains would develop preferentially in smaller particles. This finding is in agreement with the fractal comminution model developed by Sammis and Ashby (1986) which stipulates that the distribution of contacts is such that smaller grains can cushion the larger particles and shield them from tensile stress concentrations. As a result, crushing would preferentially develop in the smaller grains while larger grains remain intact. Desu and Annabattula (2019) also reported that smaller grains in a polydisperse assembly have a lower coordination number, the influence of which on the grain strength was measured by Saadi et al. (2017), who showed that grains with a higher coordination number were stronger.

Therefore, the lower critical stress values found for bidisperse and polydisperse synthetic samples (Figure 12) are likely due to the homogeneity of the monodisperse sample compared to the bidisperse and polydisperse samples. As the shape and elastic properties of all glass beads are the same, most grains in the monodisperse samples are crushed at the same critical state of stress under hydrostatic compression (Figure 12a). On the contrary, in the bidisperse and polydisperse samples, normal forces induced at the grain contacts likely reach the critical value at different values of the externally applied effective pressure, resulting in an earlier and more gradual transition to inelastic deformation for the bulk sample. This can explain some of the differences between the shape of the hydrostatic curves in Figure 12a.

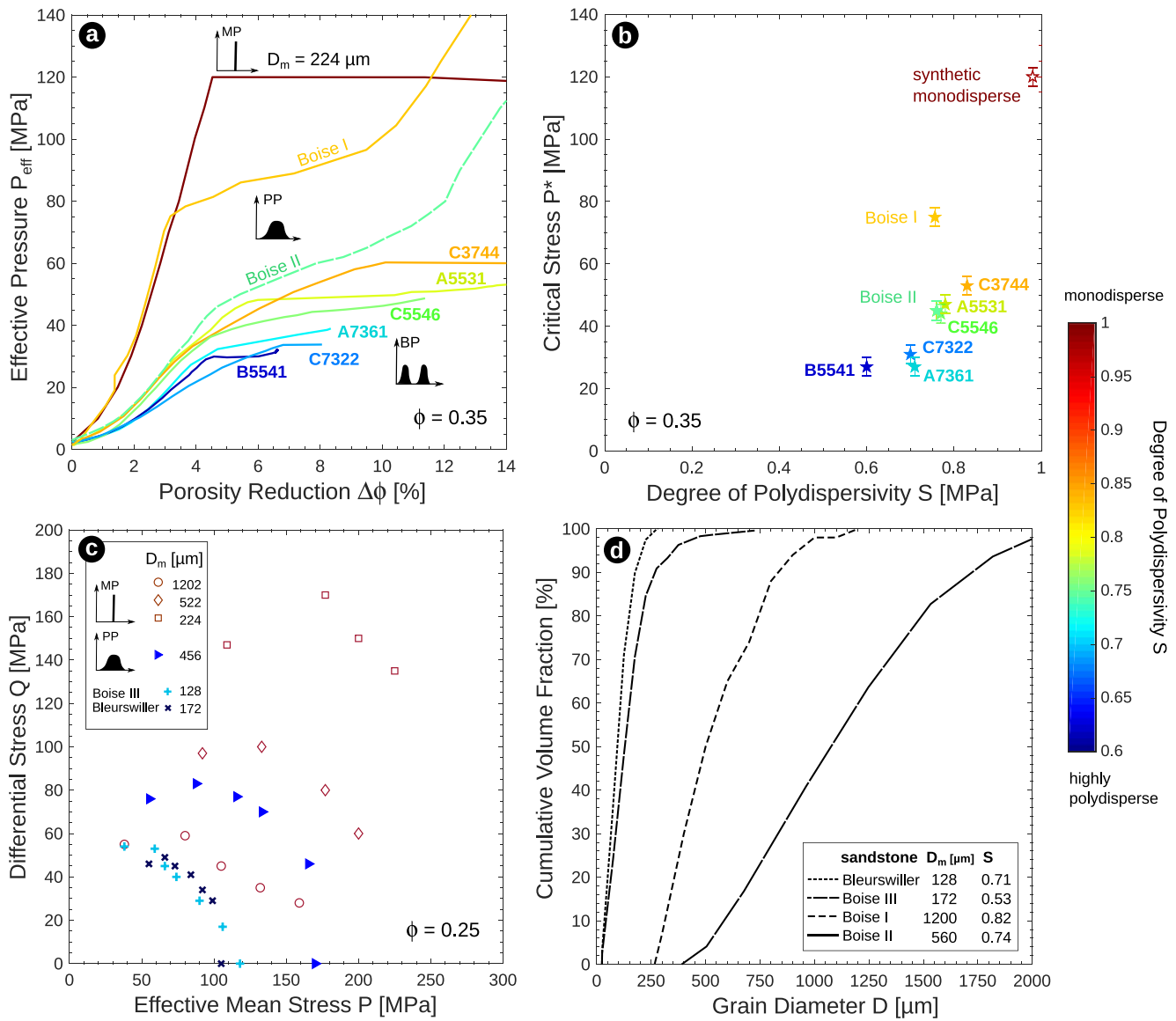


**Figure 13.** Comparison between mechanical data obtained on sintered glass bead samples and mechanical data reported for natural sandstones. (a) The hydrostatic curves of the bidisperse synthetic samples compared to that of a monodisperse synthetic sample (Carbillet et al., 2021) and of Boise I (Zhang et al., 1990) and Boise II (Baud et al., 2000) sandstones. (b)  $P^*$  values are presented as a function of the degree of polydispersity and fitted using a linear regression. (c) Critical stress values reported for monodisperse synthetic samples (Carbillet et al., 2021) and for Boise III and Bleurswiller sandstones (Cheung et al., 2012) are compiled with those for polydisperse samples. (d) The grain size distributions of the natural sandstones which our synthetic samples are compared were used to derive the mean grain diameter  $D_m$  and polydispersity  $S$ . The latter is color coded using the colorbar on the right.

### 5.2. Comparison to Natural Porous Rocks

Carbillet et al. (2021) showed that sintered glass bead samples, which can be prepared to contain independently controlled and predefined porosities and grain size distributions, are suitable analogs for natural sandstones. Therefore, we consider that the results presented in this study can be compared with those reported for natural sandstones of similar porosity to gain insights into the influence of grain size distribution on the mechanical behavior of natural porous rocks. In Figure 13, mechanical data for monodisperse, bidisperse, and polydisperse synthetic samples are compiled with mechanical data for Bleurswiller sandstone (France) and three sandstones from Boise (Idaho, USA), which we refer to as Boise I, Boise II, and Boise III. Boise I is a coarse-grained and poorly-sorted sandstone with a porosity of 0.35 that is composed of 40 vol% quartz and has a clay content of 6 vol% (Krohn, 1988). Zhang et al. (1990) studied the hydrostatic behavior of Boise I and reported a value of

75 MPa for  $P^*$  (Figure 13a). Boise II, with a similar porosity of 0.35 and composed of 67 vol% quartz and a clay content of 13 vol%, was studied by Baud et al. (2000) under both triaxial and hydrostatic compression and reported a value of 42 MPa for  $P^*$  (Figure 13a). Using thin sections of the Boise I and Boise II sandstones studied by Zhang et al. (1990) and Baud et al. (2000), respectively, we performed a grain size analysis following the method of Heap et al. (2017) to determine the grain size distributions and compute the corresponding degrees of polydispersivity. Our findings are summarized in Figure 13d. We also compare our results to those published in Cheung et al. (2012) for Bleurswiller and Boise III sandstones, both with a porosity of approximately 0.25 and very similar petrological compositions with approximately 60 vol% quartz and a clay content of 11 vol%. We determined the mean grain diameter  $D_m$  and polydispersivity  $S$  using the grain size distributions reported by Cheung et al. (2012) for these two sandstones (Figure 13d).

Comparing the hydrostatic curves of Boise I and II with those for bidisperse and monodisperse synthetic samples, several observations can be made. First, at a fixed porosity of 0.35, the stress required to reach the onset of grain crushing for Boise I is higher than that for Boise II, which are both higher than that for bidisperse synthetic samples and lower than that for a monodisperse synthetic sample. Such an observation cannot be solely explained by differences in the mean grain diameter, which was found to be a first-order control microstructural parameter by Carbillat et al. (2021). Indeed, the mean grain diameters for Boise I and Boise II were estimated to be 1,200 and 560  $\mu\text{m}$ , respectively, while the monodisperse and bidisperse samples have grain diameters of 224 and 314–998  $\mu\text{m}$ , respectively. Considering the influence of mean grain diameter only, the pressure required for  $P^*$  would be expected to be higher for Boise II than for Boise I, both being lower than that for the monodisperse synthetic sample and falling in the same range than that for the bidisperse samples. However, the complexities that arise in the compilation in Figure 13b highlight a possible influence of the degree of polydispersivity and the modality of the grain size distribution. Boise I and Boise II both have a monomodal grain size distribution (Figure 13d) but a degree of polydispersivity lower than that of the monodisperse sample ( $S = 0.98$ ) and the hydrostatic curves reported for these two natural sandstones are indeed found to fall between the those for the bidisperse and monodisperse synthetic samples. Moreover, the polydispersivity found for Boise II is 0.74 whereas it is 0.82 for Boise I, for which  $P^*$  is higher. Therefore, the compilation in Figure 13 suggests, in agreement with our results on synthetic samples, that the more monodisperse the grain size distribution, the higher the pressure required to reach  $P^*$ . The second observation is that there are important differences in the shape of the hydrostatic curves of Boise sandstones and of the monodisperse synthetic samples, especially in terms of the sharpness of the transition to inelastic compaction (i.e.,  $P^*$ ). The shape of the hydrostatic curves reported for Boise sandstones are much more comparable to those for the bidisperse samples than the monodisperse sample. As discussed in the previous section, such an observation is likely due to the heterogeneity of the microstructure of the natural sandstones and the distribution of grain-grain contacts in comparison to the highly homogeneous monodisperse synthetic sample with fewer average grain-grain contacts.

Figure 13 also includes a compilation of the compactive yield caps for polydisperse samples, monodisperse synthetic samples (Carbillat et al., 2021), and Bleurswiller and Boise III sandstones (Cheung et al., 2012). This compilation reveals that, at a fixed porosity of 0.25, the stresses required to reach inelastic compaction ( $C^*$  and  $P^*$  values) are much lower for the two natural sandstones than that for all our synthetic samples, whatever their polydispersivity. Such an observation cannot be explained by their mean grain diameters: Bleurswiller and Boise III both have lower mean grain diameters (172 and 128  $\mu\text{m}$ , respectively) than the synthetic samples, which should result, according to Carbillat et al. (2021), in higher critical stress values than those for the synthetic samples. Moreover, although Bleurswiller and Boise III have very different degrees of polydispersivity, their compactive yield caps are almost superposed. Therefore, Figure 13c also highlights the importance of other microstructural parameters, which control on the compactive strength may be stronger than that of dispersivity. Overall, although one can learn from the comparison of results found for polydisperse and bidisperse synthetic samples and for natural rocks, such comparison also emphasizes the complexity of the mechanical behavior of natural rocks. Indeed, the observations made using simplified two-phases materials for which microstructural attributes can be controlled cannot simply be transposed to natural rocks, for which multiple microstructural attributes can vary widely and simultaneously. Therefore, synthetic and numerical samples provide us with means not only to deconvolve and study the isolated influence of microstructural attributes, but also to explore the cross-property relationships (Cilli & Chapman, 2021; Torquato, 2002).



### 5.3. Compaction Localization

Compaction localization has been extensively studied in the past decades because their presence can significantly reduce rock permeability and therefore compartmentalize fluid flow (Baud et al., 2012; Olsson et al., 2002; Taylor & Pollard, 2000; Vajdova et al., 2004). Compaction bands have been observed in natural rocks in the field (Aydin & Ahmadov, 2009; Eichhubl et al., 2010; Fossen et al., 2007, 2011; Tudisco et al., 2015) but also in natural rocks deformed in the laboratory (Baud et al., 2004; Bésuelle et al., 2003; Charalampidou et al., 2013; Fortin et al., 2006; Louis, Wong, & Baud, 2007; Louis et al., 2006; Olsson, 1999; Wong et al., 2001) as well as in numerical samples submitted to compressive states of stress (Marketos & Bolton, 2009; Nguyen et al., 2016; Wang et al., 2008). Holcomb et al. (2007) reviewed the state of knowledge on localized compaction and highlighted the need for identifying the microstructural parameters that can promote or inhibit compaction localization. Before and since then, experimental studies on natural and numerical samples showed that compaction bands were more likely to develop in samples with more uniform grain size distributions and, more generally, in more homogeneous samples (Cheung et al., 2012; Das et al., 2011; Katsman et al., 2005; Louis, Baud, & Wong, 2007; Louis et al., 2009; Wang et al., 2008).

Figure 14 shows the microstructure of synthetic samples with different grain size distributions and of Bleurswiller and Boise sandstones deformed to beyond the onset of shear-enhanced compaction  $C^*$ . Discrete compaction bands can be seen in a monodisperse synthetic sample with a porosity of 0.35 and a mean grain diameter of 224  $\mu\text{m}$  (Figure 14a), in a polydisperse synthetic sample with a porosity of 0.30 and a mean grain diameter of 454  $\mu\text{m}$  (Figure 14b), and in Bleurswiller sandstone with a porosity of 0.25 and a mean grain diameter of 128  $\mu\text{m}$  (Figure 14c). Although the discrete bands in the monodisperse and polydisperse sample are 2–3 and 1–2 grains-thick, respectively, we note that the thickness of the bands is approximately 500  $\mu\text{m}$  in both samples (Figures 14a and 14b). In the polydisperse sample, the discrete bands appear to propagate not only but mostly in the smaller grains of the assembly, the size of which might therefore control the band thickness. Microstructural observations on the more polydisperse sample (Figure 14c) with a porosity of 0.25 and grain diameter of 456  $\mu\text{m}$  are somehow ambiguous: compactive deformation is found to progress as a front from both ends of the sample, within which small intersecting bands are seen between intact larger grains. Our microstructural observations are in agreement with observations previously reported for natural sandstones and results of numerical simulations of granular porous rocks. Indeed, where compaction localization is observed in natural sandstones and numerical samples, compaction bands appear to form first from the extremities of the sample and progress toward the center with increasing axial strain (Baud et al., 2004; Heap et al., 2015; Tembe et al., 2008; Townend et al., 2008; Wong et al., 2001). Using X-ray tomography and computational simulations to study compaction localization in a high-porosity limestone, Wu et al. (2020) also reported similar compaction band patterns, where compaction fronts initiate from the two ends of samples and progress toward the center with progressive axial strain increments. Delocalized cataclastic flow is observed in all the bidisperse samples (Figure 14d), whatever their degree of polydispersity. Similarly, delocalized compaction, where small grains are crushed and large grains are intact, was observed in Boise sandstone (Figure 14f; Cheung et al., 2012). Using a discrete element model for the development of compaction localization in granular rocks, Wang et al. (2008) also reported very similar results where discrete compaction bands grow in relatively homogeneous granular aggregates, more diffuse compaction localization develops in more heterogeneous assemblies and is ultimately inhibited in very heterogeneous aggregated which fail by distributed cataclastic flow. Katsman et al. (2005) observed a similar evolution in the failure micromechanics in network assemblies with either no disorder, small or large disorder.

Overall, our results suggest that there exists a continuous transition from localized to delocalized compaction as the polydispersity of the grain size distribution increases (i.e., when  $S$  decreases). Such an observation might be due to the pore space morphology, where local heterogeneities in the pore space, reduced as the width of the grain size distribution increases, act as stress concentrators and promote the growth of compaction bands. Xiong et al. (2021) reported that a high ratio between the number of macropores and micropores promotes compaction localization. Abdallah et al. (2021) also found, using digital image correlation on deformed Saint Maximin limestone samples, that porosity heterogeneities control the initiation and propagation of compaction bands, which tend to grow in the high-porosity areas of the samples. On the contrary, Baud et al. (2015) reported that the compaction bands formed in Bleurswiller sandstone propagated so as to avoid porosity clusters, which were thought to act as barriers to the growth of compaction bands. Since our synthetic samples are simplified two-phase materials, the grain and pore size distributions are intimately related via pore size functions (e.g., see Wadsworth et al., 2016). For a given mean grain size, broadly speaking, the effect of increasing the width of a



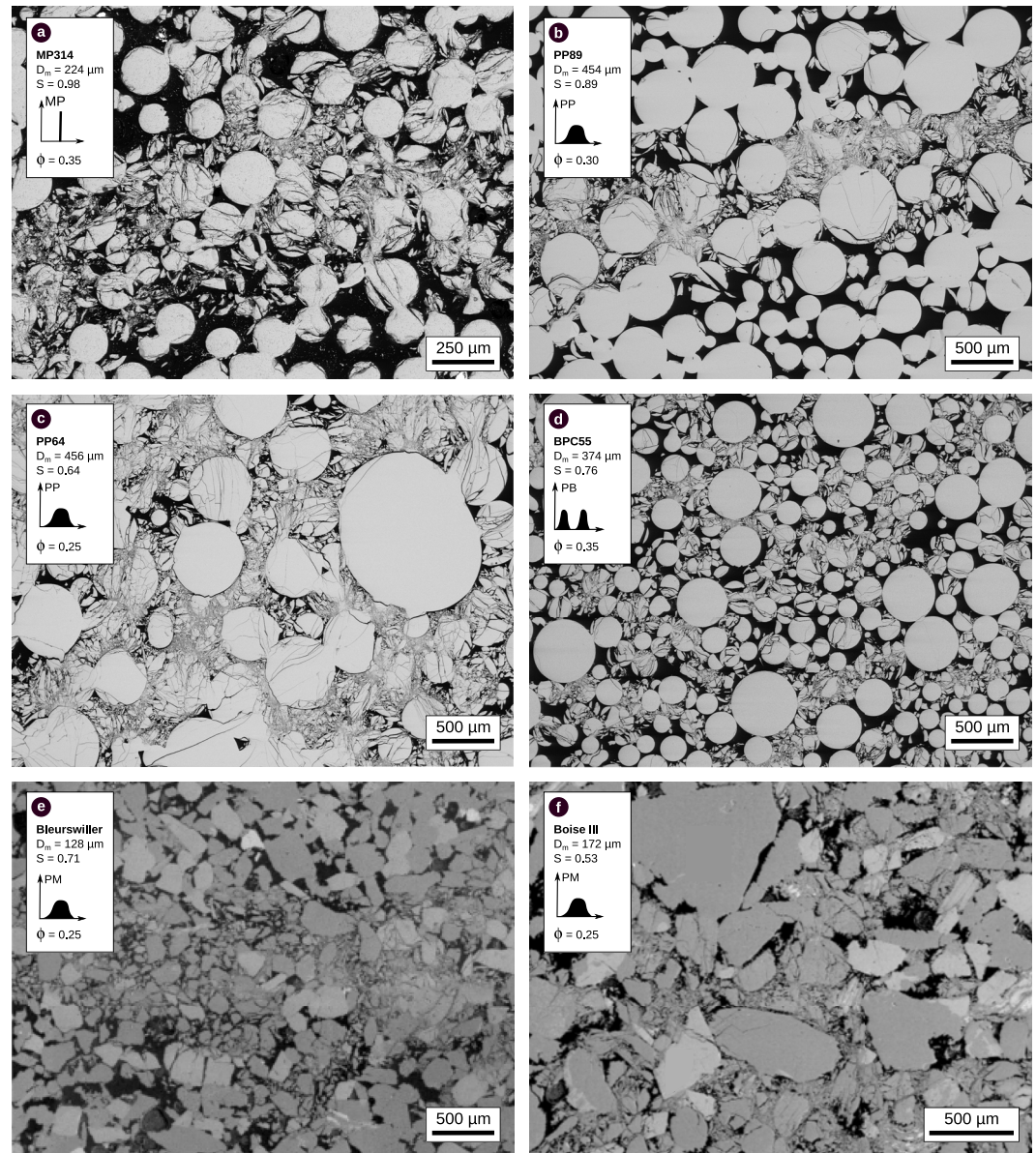


**Figure 14.** Backscattered scanning electron microscope images of the microstructure of sintered glass bead samples with (a) a monodisperse grain size distribution, (b, c) a polydisperse distribution and (d) a bidisperse distribution compared to that found in Bleurswiller and Boise sandstones (Cheung et al., 2012), after triaxial testing in the regime of shear-enhanced compaction. The type of distribution, mean grain diameter and degree of polydispersivity of each sample are indicated on the corresponding micrograph.

grain size distribution is to even further broaden the pore size distribution and to translate it to smaller mean pore sizes, relative to the situation for a monodisperse pore size distribution. This implies that continuously increasing the polydispersivity of a system of grains would distribute and tighten the pore spaces relative to a monodisperse system at the same grain size and porosity, which in turn appears to inhibit compaction band formation. However, there is clearly a fundamental difference between monomodal and bimodal polydisperse systems that cannot be captured by the  $S$  metric alone (e.g., Figure 14). Indeed, our mechanical and microstructural data for bidisperse samples do not show any evidence for compaction localization, although their degree of polydispersivity lies in the range in which compaction bands were observed in monomodal polydisperse samples. Therefore, these data highlight the fact that the parameter  $S$  underestimates the microstructural heterogeneity of the bidisperse samples in comparison to the monomodal polydisperse samples.

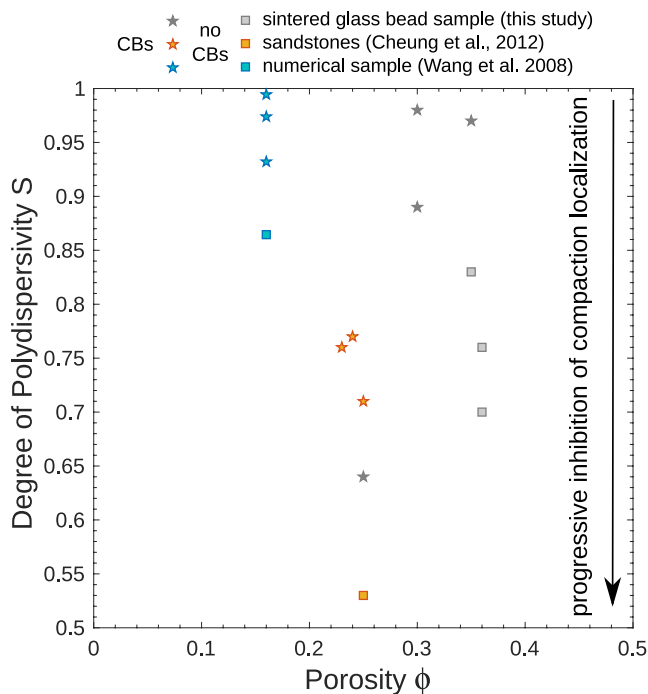


**Figure 15.** The influence of the degree of polydispersity and the porosity on the propensity for compaction localization. Results for sintered glass bead samples are compiled with that reported for numerical samples by Wang et al. (2008) and that for natural sandstones by Cheung et al. (2012).

Figure 15 presents a plot of the degree of polydispersity against porosity for samples that failed by compaction localization or by cataclastic flow. Taking into account the results of Cheung et al. (2012) for natural sandstones and Wang et al. (2008) for numerical samples, compaction bands are observed at degrees of polydispersity down to 0.71, a transitional deformation regime between discrete compaction bands and delocalized cataclasis is observed at  $S = 0.64$ , and delocalized compaction is reported at  $S = 0.53$ . Although bidisperse synthetic samples have degrees of polydispersity in the range where compaction bands would be expected, they do not exhibit any form of compaction localization. This could likely be explained by the fact that the parameter  $S$  does not encompass differences in terms of the modality of the grain size distribution and therefore underestimates the degree of heterogeneity of the microstructure of bidisperse samples. Moreover, Desu and Annabattula (2019) reported that the larger the difference in size between the grains, the stronger the effect of the grain size distribution on the contact force distributions. Thus, the effect of mixing grains with very different sizes, as is the case for the bidisperse samples, would likely always lead to the inhibition of compaction localization. Where delocalized compaction is observed (Figures 14d and 14f), it appears as though the deformation is concentrated on the smaller grains whilst larger grains remain intact. As previously discussed, such an observation might be explained by the high coordination number of larger grains in a polydisperse assembly, rendering these large grains more difficult to break.

## 6. Conclusions

Clastic sediments found in the Earth's crust are formed by the accumulation of individual minerals and rock fragments rounded by transport and sorted by deposition. However, structural heterogeneity is still encountered in these sedimentary rocks, which span a wide range of porosity, grain and pore size and shape, and/or petrological composition. Within the crust, the microstructural attributes of a clastic rock determine its mechanical response to the in-situ state of stress. Therefore, understanding the influence of microstructural parameters on the mechanical behavior and failure mode of porous crustal rocks is critical for industrial applications such as hydrocarbon and geothermal reservoir monitoring and management but also, for instance, for assessing the risk of natural hazards such as slope collapses and landslides.

In a previous study, Carbillet et al. (2021), we used sintered glass bead samples with monodisperse grain size distributions to study the influence of porosity and grain size on the mechanical compaction of porous rocks. In the present study, we extend that work using synthetic porous materials to investigate the effect of changing the type (modality) and width of the grain size distribution on mechanical behavior, while keeping other microstructural attributes constant. In the following, we provide a brief summary of our results on the influence of the grain size distribution on the mechanical behavior of porous clastic rocks.

Under both hydrostatic and triaxial compression, the stress required to reach inelastic compaction is lower for bidisperse and polydisperse synthetic samples than for monodisperse synthetic samples. We suggest that this result might be explained by changes in the morphology of the force chain network, where more uniform grain size distributions promote the formation of a more homogeneous contact force network within the microstructure, resulting in a macroscopically stronger sample.

Our microstructural data also show that compaction localization is inhibited in synthetic samples with a bidisperse grain size distribution. Indeed, we observed distributed cataclastic flow in the bidisperse samples deformed under triaxial compression, where the largest grains remained intact while the smaller grains were extensively crushed. In polydisperse samples, our microstructural observations suggest that a progressive transition might occur from compaction localization to delocalized cataclasis as the polydispersity of the grain size distribution increases. Indeed, discrete compaction bands are observed in the less polydisperse sample, in agreement with the mechanical data, while the deformation features observed in the more polydisperse sample are found in compaction fronts at both ends of the sample but within which deformation features are more diffuse. As for the

bidisperse samples, the largest grains are found to remain intact in the most deformed zones in the polydisperse samples with a high polydispersivity. These results might seem counterintuitive since the degree of polydispersivity of bidisperse samples is closer to 1 (monodisperse limit) than that of the polydisperse samples. One would therefore expect compaction localization to also occur in the bidisperse samples as well. Yet, we believe that these results actually highlight the fact that the parameter  $S$  underestimates the heterogeneity of our bimodal grain size distributions, for which compaction localization was consistently inhibited. Therefore, our results suggest that well-sorted sandstones could develop discrete compaction bands, acting as barriers for fluid flow and therefore leading to a compartmentalization of fluid flow. On the contrary, more heterogeneous and poorly-sorted sandstones would limit the development of compaction localization and thus occurrences of fluid pressurization in, for instance, hydrocarbons or geothermal reservoirs.

In this study, we attempt to understand how the grain size distribution of porous rocks may influence their mechanical behavior. Although we provide results that help sharpen our understanding of its influence, polydispersivity remains a frontier property to work with as it exists in and amongst other complex parameters. For example, changing the polydispersivity also generally changes the mean pore diameter, a key influence on mechanical behavior. Furthermore, as it is controlled by many other parameters such as the grain sphericity, grain stiffness, and packing density, a single contact force distribution can be associated with a variety of grain size distributions. We suggest that future work on synthetic materials look at the influence of other microstructural attributes such as the grain shape distribution or the cement content on the force chains network and resulting failure mode and, more generally, on the mechanical behavior of porous rocks.

### Data Availability Statement

The data supporting the manuscript's analysis and conclusions is available at <https://doi.org/10.6084/m9.figshare.20332350.v3>.

### Acknowledgments

We are grateful to Bertrand Renaudie and Christophe Nevado for the sample and thin section preparation, respectively, and to Gilles Morvan for his help using the SEM. The Boise thin section used to perform a grain size and shape analysis was kindly provided by Teng-fong Wong. The first author acknowledges funding from the Doctoral School at the University of Strasbourg. M.J. Heap acknowledges support from the Institut Universitaire de France (IUF).

### References

- Abdallah, Y., Sulem, J., Bornert, M., Ghabezloo, S., & Stefanou, I. (2021). Compaction banding in high-porosity carbonate rocks: 1. Experimental observations. *Journal of Geophysical Research: Solid Earth*, 126(1), e2020JB020538. <https://doi.org/10.1029/2020JB020538>
- Aydin, A., & Ahmadov, R. (2009). Bed-parallel compaction bands in aeolian sandstone: Their identification, characterization and implications. *Tectonophysics*, 479(3–4), 277–284. <https://doi.org/10.1016/j.tecto.2009.08.033>
- Baud, P., Klein, E., & Wong, T. (2004). Compaction localization in porous sandstones: Spatial evolution of damage and acoustic emission activity. *Journal of Structural Geology*, 26(4), 603–624. <https://doi.org/10.1016/j.jsg.2003.09.002>
- Baud, P., Meredith, P., & Townend, E. (2012). Permeability evolution during triaxial compaction of an anisotropic porous sandstone. *Journal of Geophysical Research*, 117(5), 1–23. <https://doi.org/10.1029/2012JB009176>
- Baud, P., Reuschlé, T., Ji, Y., Cheung, C. S. N., & Wong, T. (2015). Mechanical compaction and strain localization in Bleurswiller sandstone. *Journal of Geophysical Research: Solid Earth*, 120(9), 6501–6522. <https://doi.org/10.1002/2015JB012192>
- Baud, P., Wong, T., & Zhu, W. (2014). Effects of porosity and crack density on the compressive strength of rocks. *International Journal of Rock Mechanics and Mining Sciences*, 67, 202–211. <https://doi.org/10.1016/j.ijrmms.2013.08.031>
- Baud, P., Zhu, W., & Wong, T. (2000). Failure mode and weakening effect of water on sandstone. *Journal of Geophysical Research*, 105(B7), 371–389. <https://doi.org/10.1029/2000JB900087>
- Bell, F. G., & Culshaw, M. G. (1998). Petrographic and engineering properties of sandstones from the Sneinton Formation, Nottinghamshire, England. *The Quarterly Journal of Engineering Geology*, 31(1), 5–19. <https://doi.org/10.1144/GSL.QJEG.1998.031.P1.02>
- Bésuelle, P., Baud, P., & Wong, T. (2003). Failure mode and spatial distribution of damage in Rothbach sandstone in the brittle-ductile transition. *Pure and Applied Geophysics*, 160(5–6), 851–868. <https://doi.org/10.1007/PL00012569>
- Bourbie, T., & Zinszner, B. (1985). Hydraulic and acoustic properties as a function of porosity in Fontainebleau sandstone. *Journal of Geophysical Research*, 90(4), 524–532. <https://doi.org/10.1029/jb090ib13p11524>
- Brace, W. F. (1961). *Dependence of fracture strength of rocks on grain size*. OnePetro.
- Carbillet, L., Heap, M. J., Baud, P., Wadsworth, F. B., & Reuschlé, T. (2021). Mechanical compaction of crustal analogs made of sintered glass beads: The influence of porosity and grain size. *Journal of Geophysical Research: Solid Earth*, 126(4), e2020JB021321. <https://doi.org/10.1029/2020jb021321>
- Chang, C., Zoback, M. D., & Khaksar, A. (2006). Empirical relations between rock strength and physical properties in sedimentary rocks. *Journal of Petroleum Science and Engineering*, 51(3–4), 223–237. <https://doi.org/10.1016/j.petrol.2006.01.003>
- Charalampidou, E. M., Hall, S. A., Stanchits, S., Viggiani, G., & Lewis, H. (2013). Characterization of shear and compaction bands in sandstone using X-ray tomography and 3D digital image correlation. In *Advances in computed tomography for geomaterials: GeoX 2010* (pp. 59–66). <https://doi.org/10.1002/9781118557723.CH7>
- Cheung, C. S. N., Baud, P., & Wong, T. (2012). Effect of grain size distribution on the development of compaction localization in porous sandstone. *Geophysical Research Letters*, 39(21), 21302. <https://doi.org/10.1029/2012GL053739>
- Cil, M. B., & Buscarnera, G. (2016). DEM assessment of scaling laws capturing the grain size dependence of yielding in granular soils. *Granular Matter*, 18(3), 1–15. <https://doi.org/10.1007/s10035-016-0638-9>
- Cilli, P. A., & Chapman, M. (2021). Linking elastic and electrical properties of rocks using cross-property DEM. *Geophysical Journal International*, 225(3), 1812–1823. <https://doi.org/10.1093/gji/ggab046>



- Das, A., Nguyen, G. D., & Einav, I. (2011). Compaction bands due to grain crushing in porous rocks: A theoretical approach based on breakage mechanics. *Journal of Geophysical Research*, *116*(8), B08203. <https://doi.org/10.1029/2011JB008265>
- Desu, R. K., & Annabattula, R. K. (2019). Particle size effects on the contact force distribution in compacted polydisperse granular assemblies. *Granular Matter*, *21*(2), 1–12. <https://doi.org/10.1007/s10035-019-0883-9>
- Eichhubl, P., Hooker, J. N., & Laubach, S. E. (2010). Pure and shear-enhanced compaction bands in Aztec Sandstone. *Journal of Structural Geology*, *32*(12), 1873–1886. <https://doi.org/10.1016/j.jsg.2010.02.004>
- Fahy, M. P., & Guccione, M. J. (1979). Estimating strength of sandstone using petrographic thin-section data. *Bulletin of the Association of Engineering Geologists*, *16*(4), 467–485. <https://doi.org/10.2113/gseegeosci.xvi.4.467>
- Fortin, J., Stanchits, S., Dresen, G., & Guéguen, Y. (2006). Acoustic emission and velocities associated with the formation of compaction bands in sandstone. *Journal of Geophysical Research*, *111*(10), 1–16. <https://doi.org/10.1029/2005JB003854>
- Fossen, H., Schultz, R. A., Shipton, Z. K., & Mair, K. (2007). Deformation bands in sandstone: A review. *Journal of the Geological Society*, *164*(4), 755–769. <https://doi.org/10.1144/0016-76492006-036>
- Fossen, H., Schultz, R. A., & Torabi, A. (2011). Conditions and implications for compaction band formation in the Navajo Sandstone, Utah. *Journal of Structural Geology*, *33*(10), 1477–1490. <https://doi.org/10.1016/j.jsg.2011.08.001>
- Fredrich, J. T., Evans, B., & Wong, T.-F. (1990). Effect of grain size on brittle and semibrittle strength: Implications for micromechanical modeling of failure in compression. *Journal of Geophysical Research*, *95*(B7), 10907–10920. <https://doi.org/10.1029/JB095IB07P10907>
- Frenkel, J. (1945). Viscous flow of crystalline bodies under the action of surface tension. *Journal of Physics*, *9*, 385. Retrieved from <https://ci.nii.ac.jp/naid/10012829642>
- Ghazvinian, E., Diederichs, M. S., & Quey, R. (2014). 3D random Voronoi grain-based models for simulation of brittle rock damage and fabric-guided micro-fracturing. *Journal of Rock Mechanics and Geotechnical Engineering*, *6*(6), 506–521. <https://doi.org/10.1016/j.jrmge.2014.09.001>
- Guéguen, Y., & Boutéca, M. (2004). *Mechanics of fluid saturated rocks*. Elsevier Academic Press. Retrieved from [https://books.google.fr/books?hl=en&lr=&id=\\_FVt\\_dgDB-IC&oi=fnd&pg=PP1&dq=guéguen+yves&ots=sUcO2Nn\\_qz&sig=oyKs8e5n7uwAfyrWyr9Ge6BI-Sw#v=onepage&q=guéguenyves&f=false](https://books.google.fr/books?hl=en&lr=&id=_FVt_dgDB-IC&oi=fnd&pg=PP1&dq=guéguen+yves&ots=sUcO2Nn_qz&sig=oyKs8e5n7uwAfyrWyr9Ge6BI-Sw#v=onepage&q=guéguenyves&f=false)
- Guéguen, Y., & Fortin, J. (2013). Elastic envelopes of porous sandstones. *Geophysical Research Letters*, *40*(14), 3550–3555. <https://doi.org/10.1002/grl.50676>
- Guéguen, Y., & Palciauskas, V. (1994). *Introduction to the physics of rocks*. Princeton University Press.
- Guyon, E., Oger, L., & Plona, T. J. (1987). Transport properties in sintered porous media composed of two particle sizes. *Journal of Physics D: Applied Physics*, *20*(12), 1637–1644. <https://doi.org/10.1088/0022-3727/20/12/015>
- Heap, M. J., Brantut, N., Baud, P., & Meredith, P. G. (2015). Time-dependent compaction band formation in sandstone. *Journal of Geophysical Research: Solid Earth*, *120*(7), 4808–4830. <https://doi.org/10.1002/2015JB012022>
- Heap, M. J., Coats, R., Chen, C., Feng, V. N., Lavallée, Y., Kendrick, J., et al. (2018). Thermal resilience of microcracked andesitic dome rocks. *Journal of Volcanology and Geothermal Research*, *367*, 20–30. <https://doi.org/10.1016/j.jvolgeores.2018.10.021>
- Heap, M. J., Kushnir, A. R. L., Gilg, H. A., Wadsworth, F. B., Reuschlé, T., & Baud, P. (2017). Microstructural and petrophysical properties of the Permo-Triassic sandstones (Buntsandstein) from the Soultz-sous-Forêts geothermal site (France). *Geothermal Energy*, *5*(1), 26. <https://doi.org/10.1186/s40517-017-0085-9>
- Holcomb, D., Rudnicki, J. W., Issen, K. A., & Sternlof, K. R. (2007). Compaction localization in the Earth and the laboratory: State of the research and research directions. *Acta Geotechnica*, *2*(1), 1–15. <https://doi.org/10.1007/s11440-007-0027-y>
- Katsman, R., Aharonov, E., & Scher, H. (2005). Numerical simulation of compaction bands in high-porosity sedimentary rock. *Mechanics of Materials*, *37*(1), 143–162. <https://doi.org/10.1016/j.mechmat.2004.01.004>
- Krohn, C. E. (1988). Sandstone fractal and Euclidean pore volume distributions. *Journal of Geophysical Research*, *93*(B4), 3286. <https://doi.org/10.1029/JB093iB04p03286>
- Lan, H., Martin, C. D., & Hu, B. (2010). Effect of heterogeneity of brittle rock on micromechanical extensile behavior during compression loading. *Journal of Geophysical Research*, *115*(B1), 1202. <https://doi.org/10.1029/2009jb006496>
- Louis, L., Baud, P., & Rolland, A. (2009). Compaction localization in high porosity sandstones with various degrees of heterogeneity: Insight from X-ray computed tomography. In *ROCKENG09: Proceedings of the 3rd CANUS rock mechanics symposium* (Vol. 2009, pp. 1–2).
- Louis, L., Baud, P., & Wong, T. (2007). *Characterization of pore-space heterogeneity in sandstone by X-ray computed tomography* (Vol. 284, pp. 127–146). Geological Society Special Publication. <https://doi.org/10.1144/SP284.9>
- Louis, L., Wong, T., & Baud, P. (2006). X-ray imaging of compactant strain localization in sandstone. In *Advances in X-ray tomography for geomaterials* (pp. 194–198).
- Louis, L., Wong, T., & Baud, P. (2007). Imaging strain localization by X-ray radiography and digital image correlation: Deformation bands in Rothbach sandstone. *Journal of Structural Geology*, *29*(1), 129–140. <https://doi.org/10.1016/j.jsg.2006.07.015>
- Mackenzie, J. K., & Shuttleworth, R. (1949). A phenomenological theory of sintering. *Proceedings of the Physical Society Section B*, *62*(12), 833–852. <https://doi.org/10.1088/0370-1301/62/12/310>
- Marketos, G., & Bolton, M. D. (2009). Compaction bands simulated in discrete element models. *Journal of Structural Geology*, *31*(5), 479–490. <https://doi.org/10.1016/j.jsg.2009.03.002>
- Muthuswamy, M., & Tordesillas, A. (2006). How do interparticle contact friction, packing density and degree of polydispersity affect force propagation in particulate assemblies? *Journal of Statistical Mechanics: Theory and Experiment*, *2006*(9), 9003. <https://doi.org/10.1088/1742-5468/2006/09/P09003>
- Nguyen, G. D., Nguyen, C. T., Bui, H. H., & Nguyen, V. P. (2016). Constitutive modelling of compaction localisation in porous sandstones. *International Journal of Rock Mechanics and Mining Sciences*, *83*, 57–72. <https://doi.org/10.1016/j.ijrmms.2015.12.018>
- Olsson, W. A. (1974). Grain size dependence of yield stress in marble. *Journal of Geophysical Research*, *79*(32), 4859–4862. <https://doi.org/10.1029/JB079i032P04859>
- Olsson, W. A. (1999). Theoretical and experimental investigation of compaction bands in porous rock. *Journal of Geophysical Research*, *104*(B4), 7219–7228. <https://doi.org/10.1029/1998jb900120>
- Olsson, W. A., Holcomb, D. J., & Rudnicki, J. W. (2002). Compaction localization in porous sandstone: Implications for reservoir mechanics. *Oil and Gas Science and Technology*, *57*(5), 591–599. <https://doi.org/10.2516/ogst:2002040>
- Palchik, V. (1999). Influence of porosity and elastic modulus on uniaxial compressive strength in soft brittle porous sandstones. *Rock Mechanics and Rock Engineering*, *32*(4), 303–309. <https://doi.org/10.1007/s006030050050>
- Papadopoulos, L., Porter, M. A., Daniels, K. E., Bassett, D. S., & Estrada, E. (2018). Network analysis of particles and grains. *Journal of Complex Networks*, *6*(4), 485–565. <https://doi.org/10.1093/comnet/cny005>
- Paterson, M. S., & Wong, T. (2005). *Experimental rock deformation: The brittle field* (2nd ed.). Springer Verlag.

- Peng, J., Wong, L. N. Y., & Teh, C. I. (2017). Influence of grain size heterogeneity on strength and microcracking behavior of crystalline rocks. *Journal of Geophysical Research: Solid Earth*, 122(2), 1054–1073. <https://doi.org/10.1002/2016JB013469>
- Peters, J. F., Muthuswamy, M., Wibowo, J., & Tordesillas, A. (2005). Characterization of force chains in granular material. *Physical Review E: Statistical, Nonlinear and Soft Matter Physics*, 72(4), 041307. <https://doi.org/10.1103/PhysRevE.72.041307>
- Revil, A., Kessouri, P., & Torres-Verdin, C. (2014). Electrical conductivity, induced polarization, and permeability of the Fontainebleau sandstone. *Geophysics*, 79(5), D301–D318. <https://doi.org/10.1190/GEO2014-0036.1>
- Saadi, F. A., Wolf, K.-H., & van Kruijsdijk, C. (2017). Characterization of Fontainebleau sandstone: Quartz overgrowth and its impact on pore-throat framework. *Journal of Petroleum & Environmental Biotechnology*, 8, 3. <https://doi.org/10.4172/2157-7463.1000328>
- Sammis, C. G., & Ashby, M. F. (1986). The failure of brittle porous solids under compressive stress states. *Acta Metallurgica*, 34(3), 511–526. [https://doi.org/10.1016/0001-6160\(86\)90087-8](https://doi.org/10.1016/0001-6160(86)90087-8)
- Scott, T. E., & Nielsen, K. C. (1991). The effects of porosity on the brittle-ductile transition in sandstones. *Journal of Geophysical Research*, 96(90), 405–414. <https://doi.org/10.1029/90jb02069>
- Selley, R. C. (2004). Sedimentary rocks: Mineralogy and classification. In *Encyclopedia of geology* (pp. 25–37). Elsevier Inc. <https://doi.org/10.1016/B0-12-369396-9/00304-X>
- Shakoor, A., & Bonelli, R. E. (1991). Relationship between petrographic characteristics, engineering index properties, and mechanical properties of selected sandstones. *Environmental and Engineering Geoscience*, 28(1), 55–71. <https://doi.org/10.2113/gsegeosci.xxviii.1.55>
- Sulem, J., & Ouffroukh, H. (2006). Hydromechanical behaviour of Fontainebleau sandstone. *Rock Mechanics and Rock Engineering*, 39(3), 185–213. <https://doi.org/10.1007/s00603-005-0065-4>
- Taylor, W. L., & Pollard, D. D. (2000). Estimation of in situ permeability of deformation bands in porous sandstone, Valley of Fire, Nevada. *Water Resources Research*, 36(9), 2595–2606. <https://doi.org/10.1029/2000WR900120>
- Tembe, S., Baud, P., & Wong, T. (2008). Stress conditions for the propagation of discrete compaction bands in porous sandstone. *Journal of Geophysical Research*, 113(9), 1–16. <https://doi.org/10.1029/2007JB005439>
- Torquato, S. (2002). *Random heterogeneous materials: Microstructure and macroscopic properties*. Springer.
- Townend, E., Thompson, B. D., Benson, P. M., Meredith, P. G., Baud, P., & Young, R. P. (2008). Imaging compaction band propagation in Diemelt sandstone using acoustic emission locations. *Geophysical Research Letters*, 35(15), L15301. <https://doi.org/10.1029/2008GL034723>
- Tudisco, E., Hall, S. A., Charalampidou, E. M., Kardjilov, N., Hilger, A., & Sone, H. (2015). Full-field measurements of strain localisation in sandstone by Neutron tomography and 3D-volumetric digital image correlation. *Physics Procedia*, 69, 509–515. <https://doi.org/10.1016/j.phpro.2015.07.072>
- Ulusay, R., Türeli, K., & Ider, M. H. (1994). Prediction of engineering properties of a selected litharenite sandstone from its petrographic characteristics using correlation and multivariate statistical techniques. *Engineering Geology*, 38(1–2), 135–157. [https://doi.org/10.1016/0013-7952\(94\)90029-9](https://doi.org/10.1016/0013-7952(94)90029-9)
- Vajdova, V., Baud, P., & Wong, T. F. (2004). Permeability evolution during localized deformation in Bentheim sandstone. *Journal of Geophysical Research*, 109(B10), 10406. <https://doi.org/10.1029/2003JB002942>
- Vallejo, L. E., Lobo-Guerrero, S., & Chik, Z. (2005). A network of fractal force chains and their effect in granular materials under compression. In *Fractals in Engineering: New Trends in Theory and Applications* (pp. 67–80). [https://doi.org/10.1007/1-84628-048-6\\_5](https://doi.org/10.1007/1-84628-048-6_5)
- Vernik, L., Bruno, M., & Bovberg, C. (1993). Empirical relations between compressive strength and porosity of siliciclastic rocks. *International Journal of Rock Mechanics and Mining Sciences & Geomechanics Abstracts*, 30(7), 677–680. [https://doi.org/10.1016/0148-9062\(93\)90004-W](https://doi.org/10.1016/0148-9062(93)90004-W)
- Wadsworth, F. B., Vasseur, J., Llewellyn, E. W., Brown, R. J., Tuffen, H., Gardner, J. E., et al. (2021). A model for permeability evolution during volcanic welding. *Journal of Volcanology and Geothermal Research*, 409, 107118. <https://doi.org/10.1016/j.jvolgeores.2020.107118>
- Wadsworth, F. B., Vasseur, J., Llewellyn, E. W., & Dingwell, D. B. (2017). Sintering of polydisperse viscous droplets. *Physical Review E*, 95(3), 033114. <https://doi.org/10.1103/PhysRevE.95.033114>
- Wadsworth, F. B., Vasseur, J., Llewellyn, E. W., Schaubroth, J., Dobson, K. J., Scheu, B., & Dingwell, D. B. (2016). Sintering of viscous droplets under surface tension. *Proceedings of the Royal Society A: Mathematical, Physical & Engineering Sciences*, 472(2188), 20150780. <https://doi.org/10.1098/rspa.2015.0780>
- Wang, B., Chen, Y., & Wong, T. F. (2008). A discrete element model for the development of compaction localization in granular rock. *Journal of Geophysical Research*, 113(3), 1–17. <https://doi.org/10.1029/2006JB004501>
- Wasantha, P. L. P., Ranjith, P. G., Zhao, J., Shao, S. S., & Permata, G. (2015). Strain rate effect on the mechanical behaviour of sandstones with different grain sizes. *Rock Mechanics and Rock Engineering*, 48(5), 1883–1895. <https://doi.org/10.1007/s00603-014-0688-4>
- Wong, T., & Baud, P. (2012). The brittle-ductile transition in porous rock: A review. *Journal of Structural Geology*, 44, 25–53. <https://doi.org/10.1016/j.jsg.2012.07.010>
- Wong, T., Baud, P., & Klein, E. (2001). Localized failure modes in a compactant porous rock. *Geophysical Research Letters*, 28(13), 2521–2524. <https://doi.org/10.1029/2001GL012960>
- Wong, T., David, C., & Zhu, W. (1997). The transition from brittle faulting to cataclastic flow in porous sandstones: Mechanical deformation. *Journal of Geophysical Research*, 102(B2), 3009–3025. <https://doi.org/10.1029/96JB03281>
- Wu, H., Papazoglou, A., Viggiani, G., Dano, C., & Zhao, J. (2020). Compaction bands in Tuffeau de Maastricht: Insights from X-ray tomography and multiscale modeling. *Acta Geotechnica*, 15(1), 39–55. <https://doi.org/10.1007/s11440-019-00904-9>
- Xiong, L., Wu, S., & Wu, T. (2021). Effect of grain sorting, mineralogy and cementation attributes on the localized deformation in porous rocks: A numerical study. *Tectonophysics*, 817, 229041. <https://doi.org/10.1016/j.tecto.2021.229041>
- Yu, Q., Zhu, W., Ranjith, P. G., & Shao, S. (2018). Numerical simulation and interpretation of the grain size effect on rock strength. *Geomechanics and Geophysics for Geo-Energy and Geo-Resources*, 4(2), 157–173. <https://doi.org/10.1007/s40948-018-0080-z>
- Zhang, J., Wong, T.-F., & Davis, D. M. (1990). Micromechanics of pressure-induced grain crushing in porous rocks. *Journal of Geophysical Research*, 95(B1), 341. <https://doi.org/10.1029/JB095iB01p00341>
- Zhang, L., Nguyen, N. G. H., Lambert, S., Nicot, F., Prunier, F., & Djeran-Maigre, I. (2017). The role of force chains in granular materials: From statics to dynamics. *European Journal of Environmental and Civil Engineering*, 21(7–8), 874–895. <https://doi.org/10.1080/19648189.2016.1194332>
- Zhu, W., Baud, P., & Wong, T. (2010). Micromechanics of cataclastic pore collapse in limestone. *Journal of Geophysical Research*, 115(4), B04405. <https://doi.org/10.1029/2009JB006610>